

Article

# An Evaluation of the Potential for Determination of the Geographic Origin of Ruby and Sapphire Using an Expanded Trace Element Suite Plus Sr–Pb Isotope Compositions

Mandy Y. Krebs<sup>1,2,\*</sup>, Matthew F. Hardman<sup>1</sup> , David G. Pearson<sup>1</sup>, Yan Luo<sup>1</sup>, Andrew J. Fagan<sup>3</sup> and Chiranjeeb Sarkar<sup>1</sup>

<sup>1</sup> Earth and Atmospheric Sciences Department, University of Alberta, 1-26 Earth Sciences Building, Edmonton, AB T6G 2E3, Canada; mhardman@ualberta.ca (M.F.H.); gdpearso@ualberta.ca (D.G.P.); yluo4@ualberta.ca (Y.L.); chiranjeeb.sarkar@ualberta.ca (C.S.)

<sup>2</sup> Gemological Institute of America, 5355 Armada Drive, Carlsbad, CA 92008, USA

<sup>3</sup> Hummingbird Geological Services, Vancouver, BC V5Z 1R9, Canada; ajf.geoconsulting@gmail.com

\* Correspondence: mandy.krebs@nau.edu

Received: 17 April 2020; Accepted: 13 May 2020; Published: 16 May 2020



**Abstract:** The geographic origin of gem corundum has emerged as one of its major value factors. Combined with gemological observations, trace element analysis is a powerful tool for the determination of corundum provenance. However, owing to similar properties and features of gem corundum from different localities, but similar geological settings, and very low levels of many trace elements in gem corundum, the determination of geographic origin remains challenging. In this study, we present trace elements compositions determined by laser ablation inductively coupled plasma mass spectrometry (LA-ICP-MS) for rubies and blue sapphires from several different localities of geologically similar deposits: high-Fe amphibolite-type rubies, low-Fe marble-type rubies, and metamorphic blue sapphires. In addition, we determined Sr and Pb isotopic ratios by offline laser ablation sampling followed by thermal ionization mass spectroscopy (TIMS). By applying new and existing elemental discrimination schemes and the multivariate statistical method linear discriminant analysis (LDA), we show that, in addition to the commonly used discriminators Mg, Fe, V, Ti, and Ga, the elements Ni, Zr, Cr, and Zn show potential for geographic origin determination. Amphibolite-type rubies from different localities can be discriminated using Sr and Pb isotope ratios, whereas the discrimination of marble-type ruby and metamorphic blue sapphires is limited. Our results re-emphasize the challenge of geographic origin determination and the need for a more powerful discriminatory tool.

**Keywords:** geographic origin determination; ruby; sapphire; trace elements; radiogenic isotopes; linear discriminant analysis

## 1. Introduction

Gem corundum, especially the red ruby and blue sapphire varieties, are among the most valuable gemstones. The commercial value of a gem primarily depends on its size, its color, and its clarity, however, the geographic origin has recently emerged as a major factor affecting their valuation on the market [1]. This is in large part owing to the prestige attributed to certain regions (e.g., rubies from Myanmar, formerly Burma, sapphires from Kashmir), but also because of political, environmental, and ethical considerations [2,3]. Therefore, trying to identify the geographic origin of gem corundum

has developed into one of the main tasks for gem-testing laboratories, driving technological approaches to establishing accurate methods of identifying the geographic origin of gemstones.

Trace element analysis is a particularly powerful tool for the determination of gemstone provenance. Most gemological laboratories today use trace elements combined with gemological observations (e.g., inclusion characteristics and growth features) and spectroscopic analysis (Raman, Fourier transform infrared (FTIR) spectroscopy, and ultraviolet-visible-near-infrared (UV/vis-NIR) spectroscopy) to determine the country of origin [4–6]. Another technique that has proven useful for determining gem corundum provenance is the application of oxygen isotopes [7]. These approaches have proven successful in distinguishing between rubies and blue sapphires of different geological origin, however, they are not yet able to reliably distinguish between gems from different geographic regions with a similar geological formation environment [4,5,8–11]. To date, no unique fingerprinting method exists, illustrating the need for a more powerful tool for provenance determination. Determining the provenance of marble-type rubies and metamorphic blue sapphires remains particularly challenging.

Only a small number of trace elements substitute for  $Al^{3+}$  into the crystal structure: Cr, Fe, V, Ti, Mg, and Ga. All other trace elements (including Sr and Pb) in gem corundum (chemical formula  $Al_2O_3$ ) are present at ultra-trace levels and are hosted in micron to sub-micron inclusions. These micron to sub-micron inclusions may be derived during the original formation of the corundum, or from later metasomatic re-crystallization, and are either protogenetic, syngenetic, or epigenetic. In either case, the micron to sub-micron inclusion assemblage is unique for each individual deposit and as such, ultra-trace element data may provide additional discriminatory power for geographic origin determination. A recent study [12] developed a novel laser ablation inductively coupled plasma mass spectrometry (LA-ICP-MS) method for the determination of a broader spectrum of trace element compositions at quantitative levels than has been published previously. In addition to expanding the narrow range on quantifiable trace elements in ruby, Krebs et al. [12] measured Sr and Pb radiogenic isotope compositions in ruby for the first time using an offline laser ablation sampling technique followed by thermal ionization mass spectrometry (TIMS). Radiogenic isotope tracers are an attractive approach to the determination of geographic provenance because they remain largely unaffected by crystal fractionation [13].

Corundum forms in mafic and siliceous geological environments, always associated with rocks depleted in silica and enriched in alumina, because in the presence of silica, Al will be preferentially incorporated into aluminosilicate minerals such as feldspars and micas [14]. Gem corundum is rare because it also requires the presence of Cr, Fe, and Ti to substitute for Al in the structure [9,15], and thermobarometric conditions favorable for its crystallization and stability [16,17]. Two major geological environments have been found to be favorable for the generation of gem-quality corundum; amphibolite- to medium pressure granulite-facies metamorphic belts and alkaline basaltic volcanism in continental rifting environments. The global distribution of corundum deposits is closely linked to collision, rift, and subduction geodynamics, and three main periods of corundum formation are recognized worldwide [11,18,19]: (1) The Pan-African orogeny (750–450 Ma), (2) The Cenozoic Himalayan orogeny (45 Ma–Quaternary), and (3) The Cenozoic alkali basalt extrusions (65 Ma–Quaternary). Gem corundum deposits formed during these periods are often referred to as classic sources and include (1) most deposits in Southeast and Central Asia (e.g., Myanmar, Vietnam, and Afghanistan) formed during the Himalayan orogeny for marble-hosted ruby deposits; (2) Mozambique and Madagascar, among others, for metamorphic or metasomatic rubies; (3) Sri Lanka, Myanmar, and Kashmir, as well as the more modern source of Madagascar, for the metamorphic blue sapphire group; and (4) Australia, Thailand, and Cambodia for basalt-related rubies and sapphires [4,5,20]. Gem corundum deposits that formed unrelated to these periods, such as the Yogo sapphire deposit in Montana, USA (360 to 325 Ma, Ar–Ar phlogopite [21]), are referred to as “non-classical” [4]. For these types of deposits, geographic origin determination is often easier, as they can be characterized by distinct geochemical characteristics that distinguish them from other localities. Corundum deposits can be classified into primary, where the corundum is either hosted in the rock

where it crystallized, or in the rock that carried it from the zone of crystallization in the crust or mantle to the Earth's surface, and secondary, where the corundum is of detrital origin, that is, it formed in a different petrogenetic setting as where it is deposited [17]. Many of the classical gem corundum deposits are of the second type, which adds a further layer of difficulty to origin determination efforts.

In this study, we analyzed rubies and blue sapphires from several different localities of three geologically similar deposit types, amphibolite-type and marble-type rubies and metamorphic blue sapphires, using the LA-ICP-MS method of [12], to identify previously unquantifiable trace elements that show potential for geographic origin determination. In addition, Sr and Pb isotope compositions were measured for a subset of samples, and the potential usefulness of radiogenic isotopes for geographic origin determination is explored. While both LA-ICP-MS and isotope measurement approaches are currently too “destructive”, that is, visible damage and measurable weight loss are incurred, to be used on high-value client stones, our results provide further insight into gem corundum geochemistry as well as directions of focus for future method development for gemological laboratories.

## 2. Materials and Methods

### 2.1. Materials

A total of 135 gem corundum grains from 11 different locations are analyzed in this study (Figure 1, Table 1). The quality of origin determination studies heavily depends on the completeness and reliability of the reference samples used. Ideally, the samples should be collected in the deposits or mines, however, this is not always feasible because some mines are no longer active, while others are inaccessible or off limits to foreigners [22]. In this study, the samples were classified using a classification scheme developed by the Gemological Institute of America (GIA), which reflects the degree of confidence for origin determination (Table S1; the classification codes can be found in Supplementary Material S6).

The samples are divided into three groups according to their variety and known or suspected geological origin.

#### 2.1.1. Amphibolite-Type Ruby

This group comprises samples from four different localities, including the Namahaca deposit at Montepuez in Mozambique [23], the Winza deposit in Tanzania [24,25], and a deposit in the Zahamena National Park located on the Eastern coast of Madagascar [26,27]. For conventional LA-ICP-MS, a sample set provided by the American Museum of Natural History—thought to represent a deposit near Ampanihy, Toliara Province in southwestern Madagascar (George Harlow, pers. communication)—was also analyzed. However, the exact origin of this sample set could not be confirmed, and it was thus excluded from radiogenic isotope analysis. Previously published data from the Aappaluttoq deposit in SW Greenland [12] are included in the discussion, adding a fifth locality to this group.

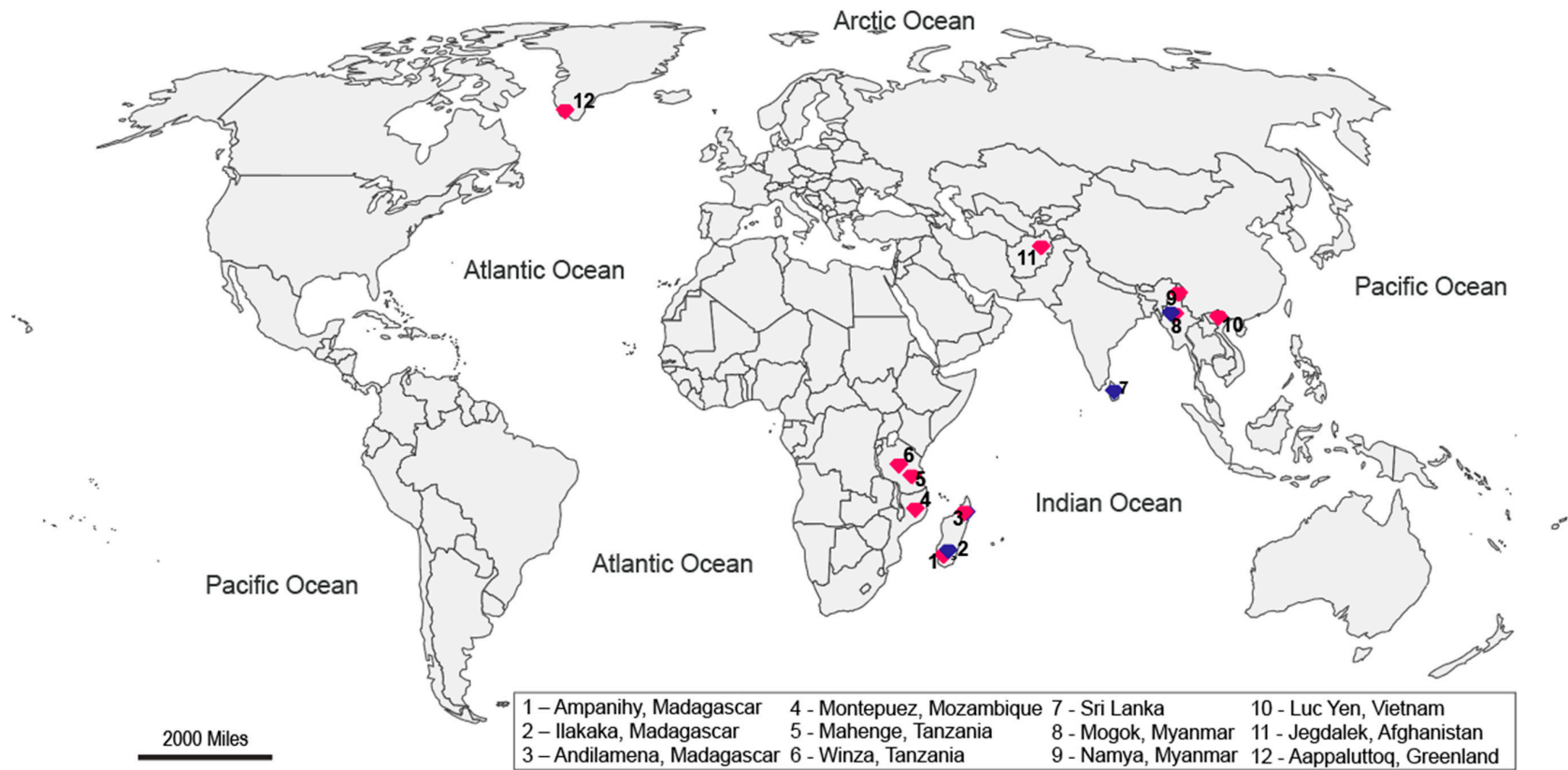


**Figure 1.** World map showing the 11 localities of origin for ruby (pink symbols) and blue sapphire (blue symbols) analyzed in this study. Also shown is a 12th locality, Greenland. Data of rubies from this locality [12] are included in the discussion.

The localities were selected based on shared features commonly found in rubies from these sources as detailed in the literature: (1) Moderate (as defined by [20]) Fe contents (in this study, between 500 to 5000 ppm); (2) Common inclusions are amphibole, mica, rutile (crystals and needles), and zircon. One exception is Winza rubies, which contain mainly amphibole, garnet, and spinel inclusions [23,25–28]; (3) The oxygen isotope ( $\delta^{18}\text{O}$ ) values overlap the mantle value, falling into the range determined for rubies formed in mafic-ultramafic rocks ( $0.25 < \delta^{18}\text{O} < 6.8\%$  [20]) [18,25,29,30]. Information on the geology of ruby host rocks remains sparse for some deposits, but, where reported, primary deposits at the localities of the amphibolite-type group were found to be associated with mafic or ultramafic rocks [25,27,30,31]; rubies in this group are thought to have formed in a desilicified host with abundant metamorphic fluids, at high pressure and temperature (at least amphibolite facies). The scope of this study is the evaluation of the usefulness of trace element and radiogenic isotope characteristics for geographic origin determination, and thus the geology and formation of amphibolite-type ruby deposits will not be discussed further. Details on current knowledge of these deposits can be found elsewhere [20,27,30,31].

**Table 1.** Samples analyzed in this study. MozX\_X samples were provided by A. Fagan, Hummingbird consulting, Vancouver. All ADXXX and four-digit samples are part of Gemological Institute of America’s (GIA) research collection. All samples named A\_XXX, V\_XXX and M\_XXX were provided by George Harlow from the American Museum of Natural History, New York.

Sample ID	Country of Origin	Location	Color	N
<i>Amphibolite-type ruby deposits</i>				
MozX_X	Mozambique (MOZ)	Montepuez, Namahaca Deposit	Pale pink–red	27
AD402, AD403, AD406–408, AD410, AD413, AD432, AD435, AD442	Tanzania (TZA)	Winza	red	10
1968, 1986, 1994, 1996, 2006, 2008, 2048, 2049	Madagascar (MDG)	Andilamena/Zahamena mining area	Red–purplish red	8
A-37145a–c, A-36928a–b, A-91729	Madagascar (MDG)	Ampanihy, Toliara	red	6
<i>Marble-hosted ruby deposits</i>				
M_112701-1–4 <sup>1</sup> ; M_110599-1–4 <sup>2</sup> ; (M_42103-1–2, 0469, 2306, 2307, 9233, 9239) <sup>3</sup> ; M_107637 <sup>4</sup> ; M_109274-1–4 <sup>5</sup>	Myanmar (MMR)	Mandalay Region: <sup>1</sup> Sagyin, <sup>2</sup> Wet Loo, <sup>3</sup> Mogok Stone Tract, <sup>4</sup> Dattaw <sup>5</sup> Kachin State: Namya	Pink–red	21
V-109310a–c, V-106502, V-109086, 0402, 1402, 2002, 2502, 3102, 4902, 6502, 7802, 8102, 8302	Vietnam (VNM)	Luc Yen	Pink–red	15
0902, 1059, 1064, 1088, 1117, 1902, 2707, 3202, 3802, 5402, 5602	Afghanistan (AFG)	Jegdalek	Pinkish red–purplish red	11
3748, 3751, 3753, 3755, 3760, 3797, 5202, 6402, 7902	Tanzania (TZA)	Mahenge, Morogoro region	Red	9
<i>Blue sapphire deposits</i>				
(AD279, AD283, AD292, AD296) <sup>1</sup> , (AD019, AD026, AD027, 4900) <sup>2</sup>	Madagascar (MDG)	<sup>1</sup> Andilamena/Andrebabe (NE), <sup>2</sup> Ilakaka (S)	Blue–dark blue	8
0098, (5210,5159) <sup>1</sup> , (AD721, AD773) <sup>2</sup> , (AD725, AD727–730) <sup>3</sup>	Myanmar (MMR)	Mogok Stone Tract; <sup>1</sup> Baw Mar mine, <sup>2</sup> Kyatpyn, <sup>3</sup> Kin	Pale blue–blue	10
1320, 1388, 6702, AD030, AD036, AD039, AD044, AD049, AD095	Sri Lanka (LKA)	Elahera	Greyish blue–blue	9

<sup>1–5</sup>: Superscript numbers match samples to their corresponding locality; N = number of samples analyzed.

### 2.1.2. Marble-Hosted Ruby

Marble-hosted rubies from four different localities, Myanmar (Mandalay Region and Namya), Vietnam (Luc Yen), Afghanistan (Jegdalek), and Tanzania (Mahenge Mountains, Morogoro Region), were selected for this study. Three of the localities, Myanmar (Mandalay Region and Namya), Vietnam (Luc Yen), and Afghanistan (Jegdalek), are from deposits where the corundum crystallized in marble as a result of retrograde isochemical reactions mainly in a closed system. Several hypotheses on the genesis of these ruby deposits have been advanced and are summarized in [20]. Rubies from Myanmar in this study are from several different areas, most of which are in the Mandalay region and include the famous Mogok Stone

Tract, Sagyin, Wet Loo, where rubies are found coating painite crystals, and Dattaw. Four samples originate from the Namya mines, located in the Kachin state, approximately 300 km north of Mogok (Figure 2).

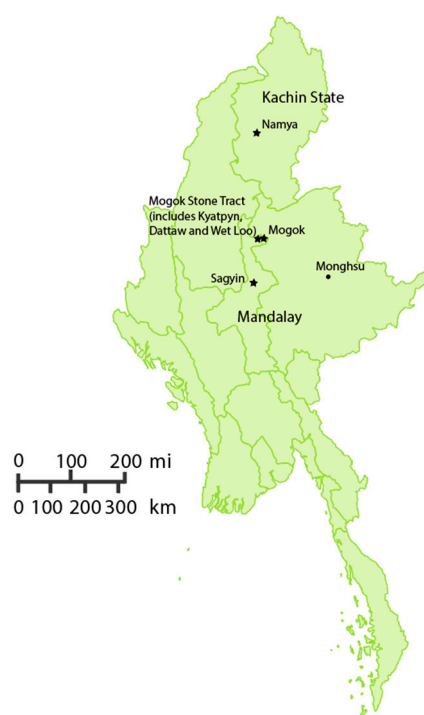


**Figure 2.** A political map showing Myanmar. Regions of origin for rubies analyzed in this study are marked by stars. Copyright © Free Vector [Maps.com](https://www.freemaps.com/).

In the course of this study, no systematic differences between the different localities were found and the samples were thus grouped together. The localities were chosen because rubies from these deposits share the following common features: (1) Low Fe contents (in this study, between ~20 and 800 ppm); (2) The most common inclusions include silk (rutile needles; to a varying degree), calcite, dolomite, apatite, spinel, zircon, and mica. In addition, salts are found as solid inclusions [20,32–35]; (3) The oxygen isotope ( $\delta^{18}\text{O}$ ) values for rubies from these localities are high, consistent with previously published values for marble-hosted ruby ( $16.3\text{‰} < \delta^{18}\text{O} < 23\text{‰}$  [7]) [35,36].

The marble-hosted ruby deposit in the Mahenge Mountains, Morogoro Region, Tanzania, is of a different type of ruby deposit associated with marble, where rubies form at the peak of prograde metamorphism in impure marble containing gneiss and silicate layers [20]. Rubies from Morogoro share similar features with those found in rubies from other marble-type deposits (e.g., Myanmar), including low Fe contents and rutile silk, spinel, zircon, and apatite inclusions [37,38]. Details on the geology and formation of marble-hosted ruby deposits have been described previously [20,38].

### 2.1.3. Metamorphic Blue Sapphires

Blue sapphires are broadly separated into two groups—“metamorphic” and “magmatic”—based on their geological origin [4,10]. Magmatic sapphires are primarily sapphires found as xenocrysts in alkali basalts, while metamorphic sapphires are primarily found in amphibolite- to medium pressure granulite-facies metamorphic belts. The majority of gem-quality metamorphic blue sapphire is found in secondary deposits, where it is of detrital origin, however, some primary deposits have been identified and are generally associated with desilicated pegmatites; skarn-related granites; marbles; gneisses; aluminous shale; and, in the case of Myanmar, syenite-like rocks associated with high-grade metamorphic rocks [5,17,20]. Metamorphic and magmatic sapphires can be separated using UV/vis-NIR spectroscopy. The spectra of the respective groups show many similarities; a major difference, however, is the presence

of a broad band around 880 nm in magmatic basalt-type sapphires, which is always more intense than the 580 nm absorption band [4]. Blue sapphires from the Baw Mar mine in Myanmar have slightly different UV/vis spectra than those from other Mogok mines; however, they are also lacking the 880 nm band visible in basalt-type sapphires [39]. This classification is not always straight-forward, however, because a recent study on blue sapphires from Madagascar has shown that heat treatment—heating the sapphires to 800–1100 °C to improve the color—may shift the spectrum from primarily having peaks between 550 and 600 nm before heating, to having a strong peak at 880 nm after heating [40].

The blue sapphire samples analyzed in this study were classified as metamorphic based on UV/vis-NIR spectroscopy and inclusion features and are from three different countries: Sri Lanka, Myanmar, and Madagascar. Samples from Sri Lanka originate from the Elahera gem field in Central Sri Lanka [41]; sapphires from Myanmar from the Mogok Stone Tract [42,43]; and sapphires from Madagascar originate from two different areas, including the secondary Ilakaka deposit in the south [44] and Andrebabe in the northeast [45].

The localities for metamorphic blue sapphires in this study were chosen because they share several common features as published in previous studies: (1) lower Fe and Ga and higher Mg than magmatic blue sapphires, that is, sapphire xenocrysts within basalts [10]; (2) common inclusions are mica (phlogopite, muscovite, biotite), rutile crystals and needles, zircon, apatite, and spinel [27,41,42,44,46–48]; and (3) high  $\delta^{18}\text{O}$  values ( $>7.7\%$ ) [7].

Details on the geology and formation of metamorphic blue sapphire deposits can be found elsewhere [7,11,17].

## 2.2. Methods

### 2.2.1. Trace Element Analysis

Trace element and radiogenic isotope compositions were determined using novel methods developed for analysis of low abundance elements in ruby at the Arctic Resources Geochemistry Laboratory, University of Alberta (Edmonton, AB, Canada) [12]. Individual grains were mounted on one inch epoxy grain mounts and polished with diamond to obtain a flat surface.

Trace element compositions were determined via LA-ICP-MS using a RESOLUTION M-50-LR (Resonetics-Australian Scientific Instruments, Canberra, Australia) 193 nm ArF Excimer laser (CompexPro 102, Coherent, Santa Clara, CA, USA) coupled to a sector-field Thermo Scientific Element XR2 mass spectrometer (Thermo Fisher Scientific, Waltham, MA, USA) operated in low mass resolution mode ( $M/\Delta M = \text{ca. } 300$ ). NIST612 was used as the primary standard. For quality control, NIST614 and NIST616 were measured every 8–10 samples (Table S2) and used as secondary standards to monitor overall instrument drift. Because the primary and secondary glass standards ablate differently from corundum, that is, they are not matrix-matched, repeat measurements were performed on corundum standard 02-1032 [49] to determine precision and, for some elements, accuracy (Table S2). We note that, at this stage, this reference material (RM) is not an internationally recognised reference material, but it is currently the only matrix-matched RM. We chose not to use it as a primary standard owing to the very limited number of elements for which it is characterised. Samples and standards were ablated with a laser spot size of 285  $\mu\text{m}$ , at a repetition rate of 20 Hz and with a fluence of  $\sim 6.6 \text{ J/cm}^2$ . These parameters result in clean, circular ablation pits with precise geometry, conducive to low levels of inter-element fractionation, as shown in Figure 2 of [12]. Helium served as the carrier gas. Each analysis consisted of 60 s gas blank acquisition, followed by 60 s ablation time and a 40 s delay for washout. Data were acquired for  $^{25}\text{Mg}$ ,  $^{29}\text{Si}$ ,  $^{39}\text{K}$ ,  $^{43}\text{Ca}$ ,  $^{49}\text{Ti}$ ,  $^{51}\text{V}$ ,  $^{52}\text{Cr}$ ,  $^{57}\text{Fe}$ ,  $^{60}\text{Ni}$ ,  $^{64}\text{Zn}$ ,  $^{65}\text{Cu}$ ,  $^{71}\text{Ga}$ ,  $^{88}\text{Sr}$ ,  $^{90}\text{Zr}$ ,  $^{93}\text{Nb}$ ,  $^{120}\text{Sn}$ ,  $^{139}\text{La}$ ,  $^{140}\text{Ce}$ ,  $^{141}\text{Pr}$ ,  $^{146}\text{Nd}$ ,  $^{165}\text{Ho}$ ,  $^{178}\text{Hf}$ ,  $^{181}\text{Ta}$ ,  $^{184}\text{W}$ ,  $^{208}\text{Pb}$ ,  $^{232}\text{Th}$ , and  $^{238}\text{U}$ , with a dwell time of 10 ms for Mg, Si, K, Ca, Ti, V, Cr, Fe, Zn, Ga, and W; a dwell time of 20 ms for Ni, Cu, Zr, Nb, La, Ce, Pr, Nd, Ho, Hf, Ta, Th, and U; and a dwell time of 30 ms for Sr, Sn, and Pb. Two spots were measured on each grain. The analyzed areas were selected randomly, the only selection criterion was the absence of visible solid inclusions, other impurities, and fractures at the 10  $\mu\text{m}$  scale. Data reduction and processing was conducted offline

using Iolite v. 3.3.2 [50] with  $^{27}\text{Al}$  (52.92 wt%) as the internal standard element. Careful screening of the time-resolved display and segment-picking for data integration in Iolite permits the identification of signal spikes from prominent inclusions, and were thus excluded during data reduction, resulting in only a single analytical run for some samples. Limits of quantification (LOQ) for all analysed elements are calculated as  $3 \times \text{LOD}$  and are listed in Table 2. Typical precision of the analyses ranges from 1% to 10% for the secondary standards ( $2\sigma$ ) and 10% to 20% ( $2\sigma$ ) for the corundum RM 02-1032. As expected, elements close to the LOQ have lower precision. The accuracy for corundum, using NIST 612 as the primary standard, could be determined for the elements Mg, Ti, V, Cr, Fe, and Ga, and is between 5% and 20% for the elements Ti, V, Cr, and Ga. For Mg and Fe, however, the accuracy is less satisfactory, with ~75% and ~35%, respectively, and illustrates the importance of using matrix-matched standards for LA-ICP-MS where possible. It is important to note that the isotopes  $^{43}\text{Ca}$  and  $^{29}\text{Si}$  have isobaric interferences,  $^{27}\text{Al}^{16}\text{O}$  and  $^{28}\text{SiH}$ , respectively, which are not reflected in the LOQ calculation and make accurate quantification of low abundances difficult. This is also reflected by the low precision of these elements for corundum RM 02-1032 (Table S2); therefore, the reported concentrations should be viewed as quantitative and are used here in a strictly comparative manner. The interference of  $^{64}\text{Ni}$  on  $^{64}\text{Zn}$  was determined to be negligible and was not corrected for.

**Table 2.** Median limits of quantification (LOQ –  $3 \times \text{LOD}$ ) obtained for 26 elements in ppb.

Element	LOQ	Element	LOQ	Element	LOQ
$^{25}\text{Mg}$	378	$^{64}\text{Zn}$	136	$^{141}\text{Pr}$	0.59
$^{29}\text{Si}$	16266	$^{65}\text{Cu}$	78	$^{146}\text{Nd}$	2.55
$^{39}\text{K}$	322	$^{71}\text{Ga}$	20	$^{165}\text{Ho}$	0.37
$^{43}\text{Ca}$	34500	$^{88}\text{Sr}$	5.5	$^{178}\text{Hf}$	1.4
$^{49}\text{Ti}$	253	$^{90}\text{Zr}$	5.1	$^{181}\text{Ta}$	0.95
$^{51}\text{V}$	14	$^{93}\text{Nb}$	1.37	$^{184}\text{W}$	1.04
$^{52}\text{Cr}$	299	$^{120}\text{Sn}$	9.9	$^{208}\text{Pb}$	3.9
$^{57}\text{Fe}$	2530	$^{139}\text{La}$	0.81	$^{232}\text{Th}$	0.4
$^{60}\text{Ni}$	112	$^{140}\text{Ce}$	0.56	$^{238}\text{U}$	0.18

### 2.2.2. Radiogenic Isotope Analysis

Of each corundum group, the cleanest samples were selected for isotope analysis—64 grains in total. Radiogenic isotope analyses were carried out using an offline laser ablation sampling technique, originally developed for the ablation of diamond [51,52], followed by thermal ionization mass spectrometry (TIMS). The technique utilizes a closed-system, custom-designed teflon laser ablation cell in which a sample is ablated, and the products are trapped, allowing the accumulation of higher volumes of analyte needed for isotope analysis. Within corundum, only few elements substitute into the crystal lattice, and Sr, Rb, Pb, Th, or U are hosted in micron to sub-micron mineral and fluid inclusions trapped within the corundum lattice instead. This technique allows us to bulk sample the micron to sub-micron mineral assemblages, and thus obtain representative isotopic ratios. Offline ablation and TIMS measurements were carried out following the protocols outlined in [12,53] and briefly summarized here.

The corundum samples were leached in 16 N Seastar ultra purity acid (UPA)-grade  $\text{HNO}_3$  on a hotplate at 100 °C for 24 h and then rinsed in 18.2  $\Omega$  MQ  $\text{H}_2\text{O}$ . Subsequently, samples were leached in 6 N HCl for another 24 h at 100 °C followed by another rinse in MQ  $\text{H}_2\text{O}$ , and finally dried at 100 °C for at least 1 h. All samples were weighed prior to the ablation. Ablations were performed using a RESolution M-50HR (Resonetics) 193 nm ArF Excimer (CompexPro 110, Coherent, Santa Clara, CA, USA) laser ablation system, in a raster pattern with the following ablation conditions: spot size 90  $\mu\text{m}$ , repetition rate 100 Hz, and fluence 4–7  $\text{J}/\text{cm}^2$ . Areas selected for ablation are free of visible inclusions and fractures, however, depending on the clarity of the samples, fractures are occasionally difficult to avoid, and larger solid inclusions may not be visible beneath the surface. Ablation times varied from 3 to 6 h.

Following ablation, 2 mL of 6 N HCl ultra purity acid (UPA) was added to the sample beaker and a Teflon cap replaced the laser window. The sealed cell was then placed in an ultrasonic bath for 40 min to loosen the material from the sample. The fluid was then transferred using a pipette from the ablation cell to a 7 mL Teflon beaker and dried on a hotplate at 100 °C. To determine the average size of the blank contribution, two to four total procedural blanks (TPBs) were collected for each batch of samples processed, using the same ablation cells and reagents used for the samples. The only step omitted was the step of ablating a solid because including an ablation step would require a solid that is essentially devoid of all trace elements or has trace element concentrations below the LOD of our method. Such a matrix has not yet been found, though we have evaluated Si-wafers for this purpose. Samples were rinsed in MQ H<sub>2</sub>O and dried before being reweighed, and the weight loss (0.02–0.42 mg) resulting from the ablation was then calculated. The dried ablation products were dissolved in 200 µL of 3 N HNO<sub>3</sub> and placed on a hot plate for approximately 2 h to homogenize. After cooling, a ~20% aliquot by volume was transferred into a pre-leached 7 mL Teflon beaker for trace element analysis and the remaining sample was processed for isotopic analysis.

Strontium was separated using Sr spec resin following procedures after [54,55]. For the Mozambique sample suite, Pb was eluted after Sr in the same column. However, semi-transparent, sticky jam-like residues in the Pb fraction lead to loading difficulties, resulting in low intensities of Pb for TIMS analysis. Therefore, for all other samples, the Pb fraction was separated in separate columns using BioRad AG1-X8 anion exchange resin (100–200 µm mesh) [12].

Total procedural blanks (TPBs) and aliquot sample solutions were analyzed for trace elements using a Thermo Scientific Element XR2 magnetic sector ICPMS (Thermo Fisher Scientific, Waltham, MA, USA) coupled with an APEX-Q high-efficiency sample introduction system (Elemental Scientific Inc., Omaha, NE, USA) fitted with a membrane desolvation module (ACM—actively cooled membrane). Each dried sample was taken up in 1 mL 3% UPA HNO<sub>3</sub>, with 500 ppt In added as internal standard. Instrumental conditions were similar to those described by [53]. The isotopes measured were as follows: <sup>55</sup>Mn, <sup>56</sup>Fe, <sup>59</sup>Co, <sup>63</sup>Cu, <sup>64</sup>Zn, <sup>69</sup>Ga, <sup>85</sup>Rb, <sup>88</sup>Sr, <sup>89</sup>Y, <sup>90</sup>Zr, <sup>93</sup>Nb, <sup>98</sup>Mo, <sup>133</sup>Cs, <sup>137</sup>Ba, <sup>139</sup>La, <sup>140</sup>Ce, <sup>141</sup>Pr, <sup>143</sup>Nd, <sup>147</sup>Sm, <sup>151</sup>Eu, <sup>157</sup>Gd, <sup>159</sup>Tb, <sup>161</sup>Dy, <sup>167</sup>Er, <sup>173</sup>Yb, <sup>175</sup>Lu, <sup>178</sup>Hf, <sup>181</sup>Ta, <sup>208</sup>Pb, <sup>232</sup>Th, and <sup>238</sup>U. Solution concentrations were measured against a five-point calibration line derived from dilutions of a synthetic rock multi-element standard solution, MES-0314-01. The standard was diluted 50,000, 100,000, 250,000, and 500,000 times, yielding concentrations in the range of 1 ppt to 35 ppb for different elements and different dilutions, thus providing an appropriate matrix-match for the samples so calibration lines did not require extrapolation into the region of sample analyte concentrations. All concentrations were normalized to the sample weight loss.

The LOQ for trace element analysis were calculated following the same procedures detailed in [53]. A total of 57 TPBs were performed for the corundum ablations, resulting in the following LOQs: the elements Cs, Pr, Sm, Eu, Gd, Tb, Dy, Ho, Er, Yb, Lu, and U are less than 1 pg; the elements Rb, Y, Nb, La, Nd, and Th are less than 5 pg; the elements Co, Ce, Hf, and Pb are less than 20 pg; the elements Sr and Ba are less than 70 pg; the elements Mn, Cu, Zr, and Mo are less than 350 pg; and the elements Fe and Zn are less than 10.4 ng.

A purified TaF<sub>5</sub> activator was used to load Sr samples to enhance Sr ionisation. Sr isotope ratios were measured on Thermo Scientific Triton Plus TIMS, equipped with nine movable Faraday cups, in static mode using 10<sup>11</sup> Ω and 10<sup>12</sup> Ω amplifiers. Multiple loads ( $n = 21$ ) of NBS987 standards of 5 and 10 ng size gave an average value of  $0.710270 \pm 92$  ( $2\sigma$ ;  $n = 21$ ) and compares well with long-term data published in other laboratories (Thirlwall, 1991), with data for similar sized loads, and with values measured in the Arctic Resources laboratory for similar sized standards. Eleven loads of dissolved BHVO-2 of 6 ng in size gave an average value of  $0.70352 \pm 17$  ( $2\sigma$ ;  $n = 11$ ), slightly higher than, but within uncertainty of, the reported average value of  $0.70348 \pm 7$  (GeoREM Database, version 27).

Lead samples were loaded with a mixture of 3.5 µL of silicic acid activator and 0.5 µL 0.1 N H<sub>3</sub>PO<sub>4</sub>, following a similar procedure as for Sr. Pb isotopic ratios were analyzed on a Triton Plus TIMS (Thermo Fisher Scientific, Waltham, MA, USA) using a single SEM in peak-hopping mode using the method

described in [56]. The average  $^{206}\text{Pb}/^{204}\text{Pb}$ ,  $^{207}\text{Pb}/^{204}\text{Pb}$ , and  $^{208}\text{Pb}/^{204}\text{Pb}$  values for NBS981 were  $16.950 \pm 0.015$ ,  $15.456 \pm 0.013$ , and  $36.856 \pm 0.027$ , respectively, based on 21 analyses, which are within uncertainty of the values published for double spike analyses of the reference material by Todt et al. [57] of  $^{206}\text{Pb}/^{204}\text{Pb} = 16.937 \pm 0.0022$ ,  $^{207}\text{Pb}/^{204}\text{Pb} = 15.492 \pm 0.0025$ , and  $^{208}\text{Pb}/^{204}\text{Pb} = 36.701 \pm 0.011$ , respectively.

### 3. Results

#### 3.1. Trace Elements

##### 3.1.1. LA-ICP-MS

The trace element results for spot analyses on polished grains are listed in Table S1. The most abundant trace elements are Fe; Ti; Ca; Mg; Ga; and, with the exception of blue sapphires, Cr. Trace elements also mostly above the LOQ (defined here as 10 standard deviations ( $\sigma$ ) above the gas blank) are V, Zn, Ni, and Pb. Other elements that are habitually above the LOQ for at least one of the groups are Si, K, Cu, Sr, Zr, Sn, La, Ce, Nd, Pr, Th, and U. Among the three gem corundum groups analyzed, marble-hosted rubies are the purest, that is, the number of elements >LOQ is the most limited. In Table 3, the trace elements relevant or with the potential to be useful for origin determination are summarized.

**Table 3.** Trace element comparative ranges with medians in parentheses. All data are in ppm ( $\mu\text{g/g}$ ).

Sample	$^{25}\text{Mg}$	$^{49}\text{Ti}$	$^{51}\text{V}$	$^{52}\text{Cr}$	$^{57}\text{Fe}$	$^{60}\text{Ni}$	$^{64}\text{Zn}$	$^{71}\text{Ga}$
<i>Amphibolite-type ruby deposits</i>								
<b>MOZ</b> <i>n</i> = 54	18–67 (38)	21–104 (42)	2.9–8.5 (4.1)	1119–9190 (1812)	688–1522 (1001)	0.4–3.2 (1)	0.3–5.6 (0.8)	17–36 (22)
<b>TZA, Winza</b> <i>n</i> = 19	6.4–128 (91)	16–584 (99)	0.9–8 (3.1)	526–2850 (991)	1648–3937 (3204)	0.4–9.7 (6.6)	0.2–1 (0.6)	16–44 (34)
<b>MDG, Zahamena</b> <i>n</i> = 13	48–103 (78)	73–149 (109)	29–59 (37)	1782–8770 (2839)	1878–3521 (2940)	0.3–3.5 (0.8)	0.3–1 (0.4)	49–101 (64)
<b>MDG, Ampanihy</b> <i>n</i> = 12	13–40 (27)	21–86 (42)	26–49 (32)	1704–2679 (2189)	2720–3560 (3095)	0.5–2.7 (0.8)	0.4–1.4 (0.8)	84–112 (97)
<i>Marble-hosted ruby deposits</i>								
<b>MMR</b> <i>n</i> = 40	13–129 (61)	35–207 (109)	46–1074 (310)	772–6850 (2352)	23–267 (101)	0.2–2.6 (0.6)	0.2–1.8 (0.5)	12–192 (131)
<b>VNM</b> <i>n</i> = 39	12–161 (39)	36–627 (126)	8–480 (63)	242–8190 (875)	20–718 (122)	0.1–3.9 (0.4)	0.2–1.3 (0.4)	9.3–133 (58)
<b>AFG</b> <i>n</i> = 23	26–144 (59)	47–367 (111)	16–210 (82)	1267–9507 (3145)	41–679 (81)	0.07–3.2 (0.6)	0.2–1.9 (0.5)	33–92 (48)
<b>TZA, Morogoro</b> <i>n</i> = 19	42–162 (71)	84–360 (126)	15–212 (34)	462–2319 (1207)	128–1250 (449)	0.08–1.7 (0.2)	0.2–0.6 (0.4)	42–117 (60)
<i>Blue Sapphire deposits</i>								
<b>MDG, Andrebabe</b> <i>n</i> = 7	6.4–44 (19)	22–35 (26)	1.8–7 (3.6)	2.7–11 (5.4)	2218–4975 (3460)	0.2–4.2 (1.9)	0.3–3.1 (1.3)	125–216 (159)
<b>MDG, Ilakaka</b> <i>n</i> = 6	21–133 (63)	41–841 (164)	12–34 (23)	2.2–20 (6)	804–2136 (924)	0.09–0.4 (0.23)	0.25–0.75 (0.5)	50–233 (63)
<b>LKA</b> <i>n</i> = 18	28–146 (63)	50–283 (138)	3.8–62 (9.4)	0.9–4.9 (1.8)	497–2402 (997)	0.8–1.9 (0.33)	0.1–0.9 (0.3)	46–131 (97)
<b>MMR</b> <i>n</i> = 20	5.8–77 (25)	8.7–275 (59)	0.5–27 (1.5)	1.6–9.8 (2.6)	1186–5617 (2040)	0.4–3.2 (1)	0.1–1.3 (0.5)	51–193 (89)

The trace element characteristics of the two ruby groups are consistent with those previously reported in the literature [20]: moderate contents of Cr (<1 wt%), low Ga (<130 ppm), and low Ti (~16–630 ppm) for all rubies, moderate contents of Fe for amphibolite-type rubies (~700–4000 ppm), low Fe for marble-hosted rubies (~20–1250 ppm), and low V for amphibolite-type rubies (~1–60 ppm) compared with elevated V for marble-hosted rubies (~8–1074 ppm). Among amphibolite-type rubies,

some differences in trace element abundance are observed, including higher median V and Ga contents for rubies from Madagascar (medians of V = 37 and Ga = 64 ppm in the north, and V = 32 and Ga = 97 ppm in the south) than for Mozambique (medians of V = 4.1 and Ga = 22 ppm) and Tanzania (medians of V = 3.1 and Ga = 34 ppm) rubies. Rubies from Tanzania and Zahamena, MDG have approximately twice as much Mg and Ti as those from Mozambique and Ampanihy, MDG. In addition, Mozambique rubies analyzed in this study have lower Fe (median = 1001 ppm) than rubies from the other amphibolite-type deposits (median ~3000 ppm), while Winza, TZA rubies are characterized by higher Ni contents (median = 6.6 ppm vs. max ~1 ppm for the other the deposits). Among the marble-hosted rubies, rubies from Myanmar have higher V (median = 310 ppm) and Ga (median = 131 ppm) than rubies from the other localities, while rubies from Morogoro, TZA have the lowest V contents (median = 34 ppm), which overlap with the highest V values in the amphibolite-type deposits, and are also characterized by higher Fe contents (median = 449 vs. median = 81–122 ppm for the other deposits). Differences in trace elements of blue sapphires from different deposits are as follows: sapphires from Andrebabe, MDG, and Myanmar have lower Mg, Ti, and V, and higher Fe and Ni contents than Ilakaka, MDG and Sri Lanka sapphires. Both Madagascar sample suites have higher Cr contents than Sri Lanka and Myanmar samples. Blue sapphires from Andrebabe, MDG are further characterized by higher Ga contents. Overall, the trace element contents of the blue sapphire samples analyzed in this study exhibit trace element characteristics typical for metamorphic blue sapphires reported by [10], including low Ga/Mg ratios (<10).

### 3.1.2. Solution ICP-MS

For 64 rubies and sapphires, a fraction of the offline ablated material was analyzed for trace elements using solution ICP-MS. This comprised 17 amphibolite-type rubies (five from Zahamena, MDG; eight from Mozambique; and four from Winza, TZA), 24 marble-type rubies (10 from Myanmar; five from Vietnam; five from Afghanistan; and four from Morogoro, TZA) and 22 metamorphic blue sapphires (seven from Sri Lanka; eight from Myanmar; four from Ilakaka, MDG; and three from Andrebabe, MDG). For five samples, multiple offline ablations were performed to examine homogeneity and look for isotopic variations within single crystals.

The elemental abundances of all analyzed samples for rare earth elements (REEs), high field strength elements (HFSEs), and large ion lithophile elements (LILEs) range from low ppb levels up to 100s of ppm in some cases (Table S3). When normalized to primitive mantle values [58], most samples show enrichment of LILE and HFSE over LREE and Nb, a positive  $Pb_N$  anomaly (relative to  $Ce_N$  and  $Pr_N$ ) and LREE enrichment relative to HREE ( $La_N/Yb_N \sim 1.5\text{--}991$ ) (Figure 3).

Except for the Mozambique and Zahamena, MDG suites, all  $Y_N$  anomalies (relative to  $Dy_N$  and  $Ho_N$ ) are not real, but are caused by single extremely high values in the Vietnam and Ilakaka, MDG datasets (Figure 3c,d). Eu anomalies ( $Eu/Eu^* = 2 \times Eu_N/(Sm + Gd)_N$ ) are mostly negative, with only rubies from Mozambique showing  $Eu/Eu^* > 1$  (Figure 4a), while Ce anomalies are typically  $\geq 1$  (Figure 4d). Sr anomalies for rubies are mostly positive—exceptions are the majority of the amphibolite-type Mozambique and some marble-type Myanmar rubies, while all blue sapphires have  $Sr/Sr^* < 1$  (Figure 4c). It is also noteworthy that Sr is <LOQ in all rubies from Zahamena, MDG. Ta/Nb ratios are predominantly  $>1$  for all deposit groups (Figure 5a–c), while the U/Pb ratios range are mostly  $<1$  for amphibolite-type rubies,  $>1$  for marble-type rubies, and range from  $U/Pb_N = 0.01$  to 20 for metamorphic blue sapphires (Figure 5d–f). Rubies mostly have  $Th/U < 1$ , with the exception of amphibolite-type Mozambique rubies, most of which have  $Th/U < 1$  (Figure 5g–i).

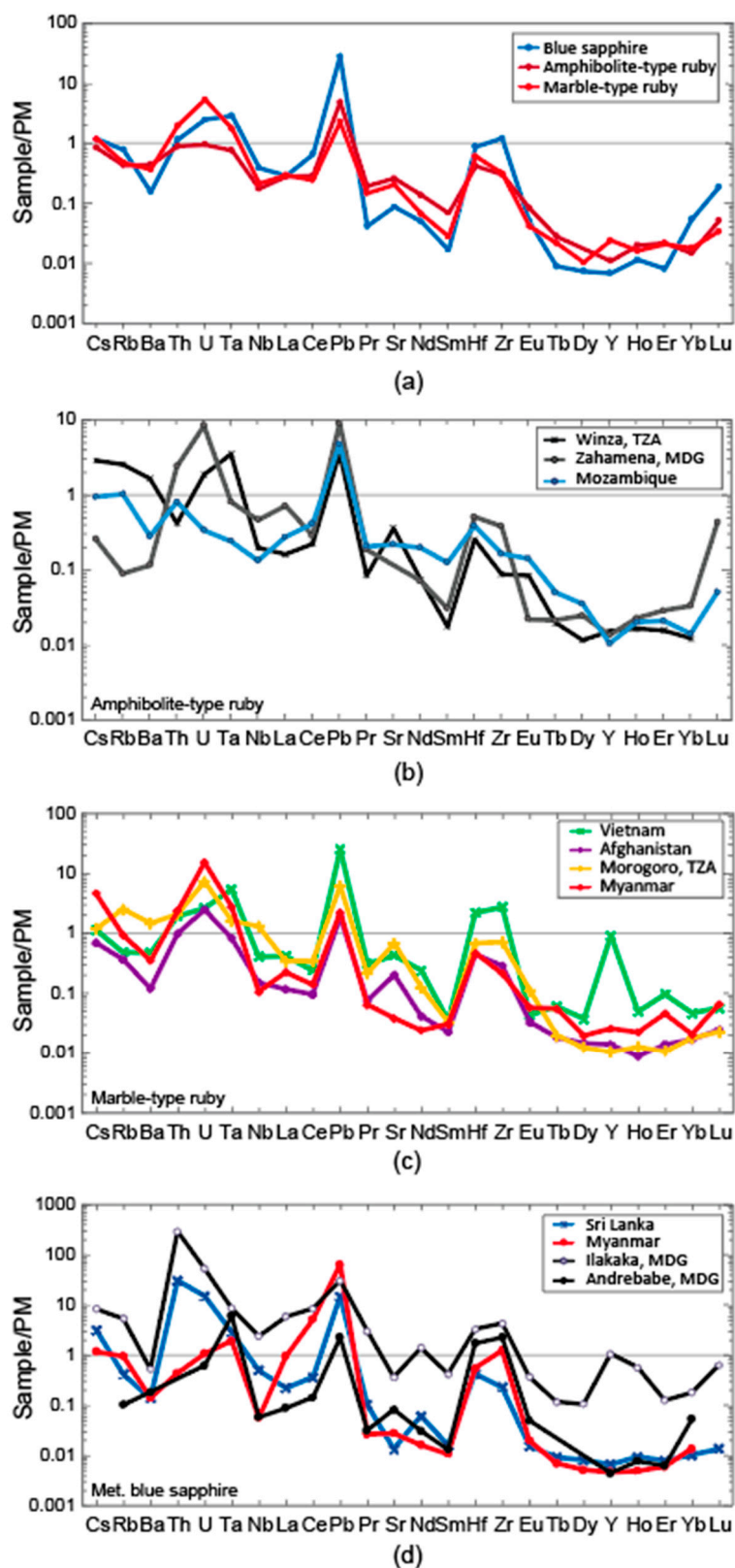


**Figure 3.** Primitive mantle (PM)-normalized [58] median trace element concentrations in (a) the three different deposit groups, (b) the amphibolite-type ruby localities, (c) the marble-type ruby localities, and (d) the localities of metamorphic blue sapphire analyzed by offline ablation followed by solution inductively coupled plasma mass spectrometry (ICPMS) in this study. All data plotted are >limit of quantification (LOQ). TZA, Tanzania; MDG, Madagascar.

Most blue sapphires have  $\text{Th} < \text{LOQ}$ , but where  $\text{Th} > \text{LOQ}$ ,  $\text{Th}/\text{U}$  is predominantly  $< 1$ . Zr and Hf, more often  $> \text{LOQ}$  in ruby than in blue sapphire, are enriched with Zr/Hf less than or greater than 1 (Figure 5j–l).

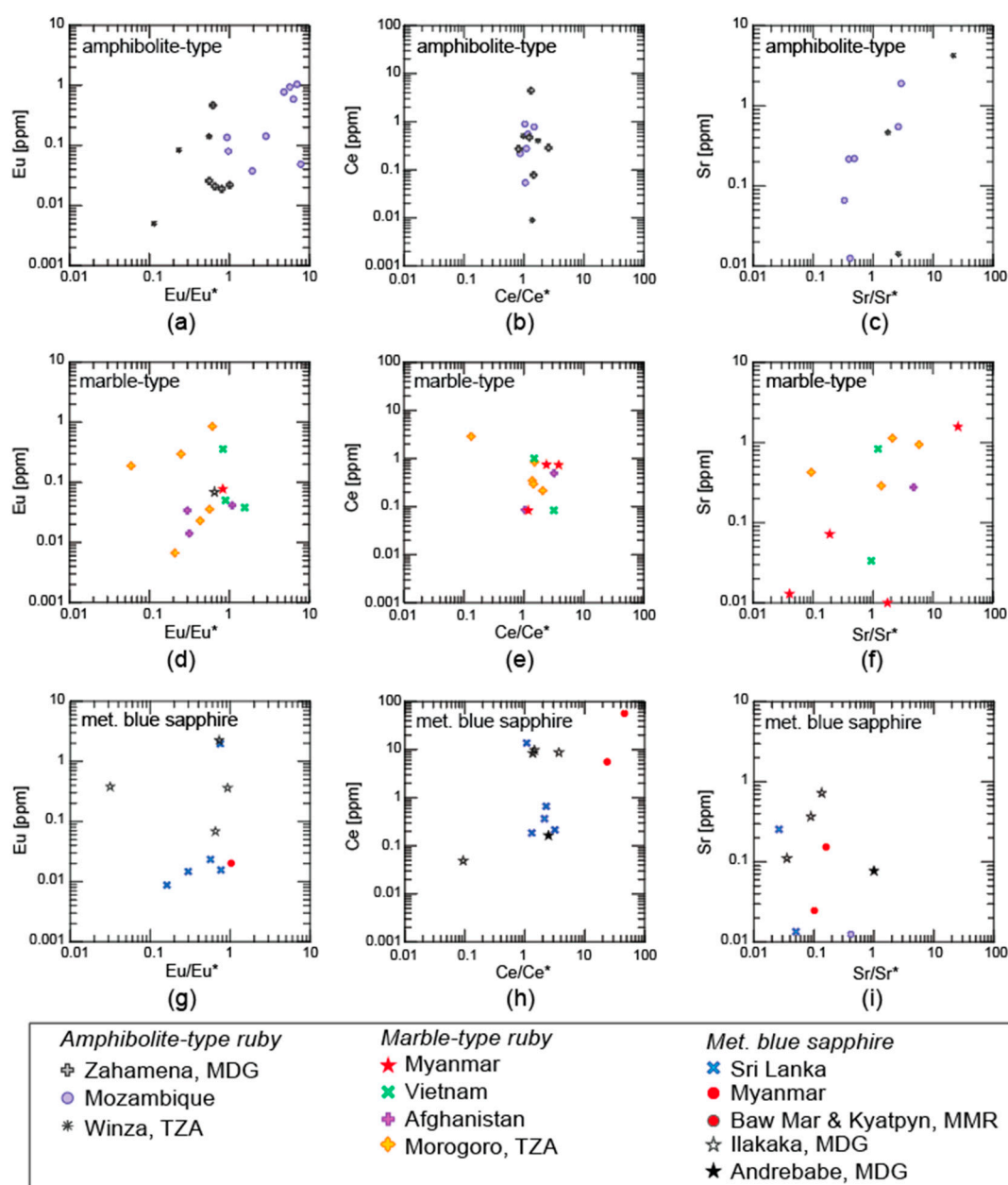


**Figure 4.** Primitive mantle-normalized [58] trace element compositions in gem corundum ablated offline in this study. Points represent individual analyses. (a–c) Eu versus  $\text{Eu}/\text{Eu}^*$ , (d–f) Ce versus  $\text{Ce}/\text{Ce}^*$ , and (g–i) Sr versus  $\text{Sr}/\text{Sr}^*$ . Anomalies were calculated using  $\text{Eu}/\text{Eu}^* = 2 \times \text{Eu}_N/(\text{Sm} + \text{Gd})_N$ ,  $\text{Ce}/\text{Ce}^* = \text{Ce}_N/((\text{La}_N)^{0.667} \times (\text{Nd}_N)^{0.333})$ , and  $\text{Sr}/\text{Sr}^* = 2 \times \text{Sr}/(\text{Ce} + \text{Nd})$ , where N indicates normalization to average primitive mantle values of [58]. MNR, Myanmar.

Some differences between the different localities within each group are apparent. Among amphibolite-type ruby deposits, only the Mozambique suite is characterized by  $\text{Eu}/\text{Eu}^* > 1$  (Figure 4a) and  $\text{Th}/\text{U}$  ratios  $> 1$  (Figure 5g). In addition, Zr and Hf in Mozambique rubies are predominately  $< \text{LOQ}$ —a characteristic also seen in the LA-ICP-MS data (Figure A2). Furthermore, rubies from Winza, TZA are characterized by positive Gd anomalies; rubies from Zahamena, MDG are characterized by the absence of Sr; and both the Zahamena, MDG and Mozambique suites show Lu enrichment (Figure 3b).

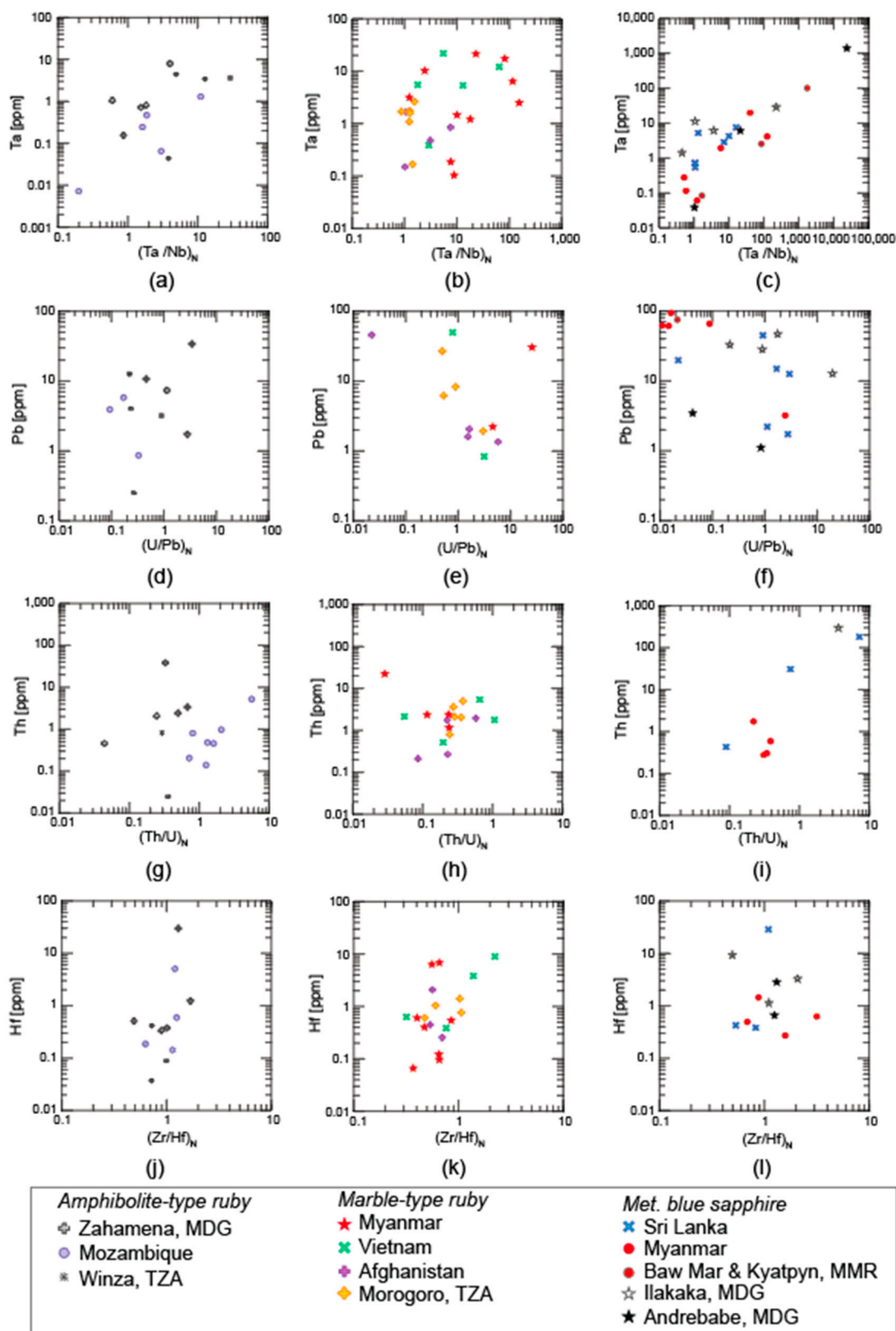


**Figure 5.** Primitive mantle-normalized [58] trace element compositions in offline ablated gem corundum analyzed in this study. Points represent individual analyses. (a–c) Ta versus  $(Ta/Nb)_N$ ; (d–f) Pb versus  $(U/Pb)_N$ , (g–i) Th versus  $(Th/U)_N$ , and (j–l) Hf versus  $(Zr/Hf)_N$  for amphibole-type ruby, marble-type ruby, and met. blue sapphire, respectively.

Trace element characteristics in offline-ablated marble-type rubies are mostly similar. However, different characteristics are apparent and include mostly very high Ta/Nb for Myanmar and Vietnam rubies versus Ta/Nb  $\sim 1$  for Morogoro, TZA rubies, and Sr/Sr\*  $< 1$  for Myanmar rubies (Figures 3, 4c and 5b).

Among the different suites of metamorphic blue sapphires, several differences are observed. Blue sapphires from Sri Lanka and Ilakaka, MDG are very similar to each other, with U/Pb mostly  $> 1$  and U (and Th where present) enrichment over Ta. Myanmar blue sapphires, on the other hand, show U/Pb  $< 1$  (Figure 5f). In addition, in Myanmar and Andrebabe, MDG sapphires, Cs is mostly  $< \text{LOQ}$ , whereas in sapphires from Sri Lanka and Ilakaka, MDG, Cs is  $> \text{LOQ}$  (Table S3).

Figure 6 shows the primitive mantle-normalized trace element patterns of the samples for which two separate offline ablations were performed to investigate the reproducibility of the data.

The trace element patterns of the two repeat analyses are remarkably similar for all samples, however, in some samples, variations for single elements are observed. For ruby moz2\_2, for instance, Sr and Ba vary, while for blue sapphire 0098 from Myanmar, Sr and Ta of the two analyses are different, and one analysis of ruby moz1\_4 shows a negative Tb anomaly. The observed variations in concentrations probably reflect different densities of inclusions, while differences in the trace element patterns of the replicates indicate that the composition of the micron to submicron inclusion assemblage varied in the ablated areas.

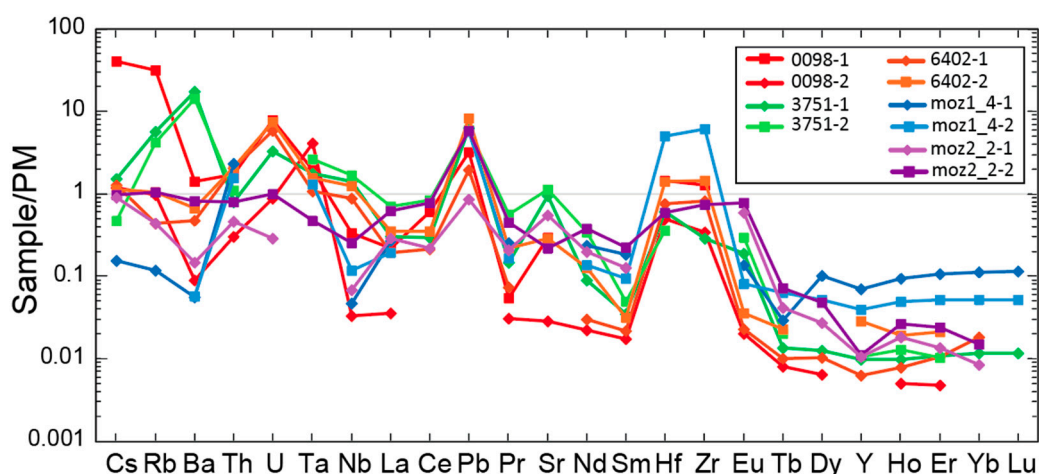


**Figure 6.** Primitive mantle-normalized [58] trace element concentrations of duplicate offline-ablations for five samples in this study. Lines of the same color denote replicate analyses of the same sample in a different area of the crystal. Sample 0098 is from the Mogok Stone Tract, Myanmar; samples 3751 and 6402 are from the Morogoro region in Tanzania; and samples moz1\_4 and moz2\_2 are from the Montepuez area in Mozambique.

### 3.2. Radiogenic Isotopes

#### 3.2.1. Sr Isotopic Composition

Gem corundum from different locations and deposit types span a wide range of Sr isotopic compositions (Table 4 and Table S3). Sr isotopic ratios of the amphibolite-type rubies (21 analyses—three duplicate) span a range between  $^{87}\text{Sr}/^{86}\text{Sr} = 0.7071 \pm 0.0005$  and  $^{87}\text{Sr}/^{86}\text{Sr} = 0.7463 \pm 0.0042$ . Within this group, rubies from Zahamena, MDG are the most radiogenic and have the widest range ( $^{87}\text{Sr}/^{86}\text{Sr} = 0.7115 \pm 0.0035$  to  $^{87}\text{Sr}/^{86}\text{Sr} = 0.7463 \pm 0.0042$ ), while rubies from Winza, TZA are the most unradiogenic and define a narrow range between  $^{87}\text{Sr}/^{86}\text{Sr} = 0.7071 \pm 0.0006$  and  $^{87}\text{Sr}/^{86}\text{Sr} = 0.7101 \pm 0.0014$  with rubies from Mozambique falling in between (Figure 7b, Table 4). For three of the Mozambique rubies, two replicate analyses were conducted, with Sr isotopic compositions for moz2\_2 of  $^{87}\text{Sr}/^{86}\text{Sr} = 0.7089 \pm 0.0030$  and  $^{87}\text{Sr}/^{86}\text{Sr} = 0.7075 \pm 0.0006$ , for moz2\_6 of  $^{87}\text{Sr}/^{86}\text{Sr} = 0.7148 \pm 0.0009$  and  $^{87}\text{Sr}/^{86}\text{Sr} = 0.7108 \pm 0.0007$ , and for moz2\_8 of  $^{87}\text{Sr}/^{86}\text{Sr} = 0.7164 \pm 0.0005$  and  $^{87}\text{Sr}/^{86}\text{Sr} = 0.7112 \pm 0.0009$ . For sample

moz2\_2, the analyses are within error of one another. For samples moz2\_6 and moz2\_8, however, the  $^{87}\text{Sr}/^{86}\text{Sr}$  ratios of the duplicate ablations are outside of their respective uncertainty intervals, indicating Sr isotopic heterogeneity that is likely controlled by the ablation of larger inclusions [12].

The range in  $^{87}\text{Sr}/^{86}\text{Sr}$  isotope ratios for the marble-type rubies ( $^{87}\text{Sr}/^{86}\text{Sr} = 0.7059 \pm 0.0007$  to  $^{87}\text{Sr}/^{86}\text{Sr} = 0.7182 \pm 0.0021$ , median  $^{87}\text{Sr}/^{86}\text{Sr} \sim 0.7082$ ) is much narrower and more unradiogenic than that of both the amphibolite-type rubies (median  $^{87}\text{Sr}/^{86}\text{Sr} \sim 0.7113$ ) and the metamorphic blue sapphires (median  $^{87}\text{Sr}/^{86}\text{Sr} \sim 0.7156$ ) (Figure 7a). Among the different localities of marble-hosted ruby, rubies from Myanmar have a more radiogenic distribution (median  $^{87}\text{Sr}/^{86}\text{Sr} \sim 0.7099$ ) and the widest range, while including both the most and least radiogenic marble-hosted ruby samples (Figure 7c). Rubies from Afghanistan; Morogoro, TZA; and Vietnam are less radiogenic, with median  $^{87}\text{Sr}/^{86}\text{Sr}$  of  $\sim 0.7083$ ,  $\sim 0.7070$ , and  $\sim 0.7063$ , respectively. For two rubies from Morogoro, TZA, two ablations and subsequent Sr isotope analyses were performed, with Sr isotopic ratios of  $^{87}\text{Sr}/^{86}\text{Sr} = 0.7081 \pm 0.0005$  and  $^{87}\text{Sr}/^{86}\text{Sr} = 0.7063 \pm 0.0030$  for sample 3751 and  $^{87}\text{Sr}/^{86}\text{Sr} = 0.7072 \pm 0.0029$  and  $^{87}\text{Sr}/^{86}\text{Sr} = 0.7093 \pm 0.0047$  for sample 6402. For both samples, the duplicate analyses are within uncertainty of each other.

**Table 4.** Ranges in Sr and Pb isotopic ratios for the different localities analyzed in this study. Number of analyses in parentheses.

Sample	$^{87}\text{Sr}/^{86}\text{Sr}$	$^{206}\text{Pb}/^{204}\text{Pb}$	$^{207}\text{Pb}/^{204}\text{Pb}$	$^{207}\text{Pb}/^{206}\text{Pb}$	$^{208}\text{Pb}/^{206}\text{Pb}$
<i>Amphibolite-type deposits</i>					
MOZ	0.7075–0.72 (n = 12)	17.86–19.00 (n = 4)	15.33–15.60 (n = 4)	0.8305–0.8655 (n = 4)	2.0292–2.0955 (n = 4)
TZA, Winza	0.7071–0.7101 (n = 4)	16.88–17.57 (n = 3)	15.57–15.62 (n = 3)	0.8880–0.9223 (n = 4)	2.1290–2.1786 (n = 3)
MDG, Zahamena	0.7115–0.7463 (n = 4)	15.92–24.64 (n = 4)	15.21–15.99 (n = 4)	0.6488–0.9539 (n = 4)	1.5866–2.8679 (n = 4)
<i>Marble-hosted deposits</i>					
MMR	0.7059–0.7182 (n = 8)	18.02–19.75 (n = 9)	15.55–15.72 (n = 9)	0.7959–0.8636 (n = 9)	1.9643–2.1037 (n = 9)
VNM	0.7062–0.7066 (n = 3)	18.11–19.08 (n = 3)	15.50–15.64 (n = 3)	0.8177–0.8558 (n = 3)	2.0223–2.0819 (n = 3)
AFG	0.7059–0.7089 (n = 5)	17.77–19.13 (n = 5)	15.48–15.67 (n = 5)	0.8196–0.9721 (n = 5)	2.0090–2.1081 (n = 5)
TZA, Morogoro	0.7063–0.7093 (n = 5)	17.38–35.86 (n = 4)	15.39–16.57 (n = 4)	0.4616–0.8858 (n = 4)	1.0561–2.1320 (n = 4)
<i>Blue sapphire deposits</i>					
MDG, Andrebabe	0.7066–0.7087 (n = 2)	17.08–18.30 (n = 3)	15.47–15.57 (n = 3)	0.8505–0.9056 (n = 3)	2.1113–2.1484 (n = 3)
MDG, Ilakaka	0.7156–0.7316 (n = 4)	17.45–20.01 (n = 4)	15.54–15.80 (n = 4)	0.7895–0.8899 (n = 4)	2.0243–2.5975 (n = 4)
LKA	0.7081–0.7316 (n = 7)	17.24–20.69 (n = 7)	15.49–15.95 (n = 7)	0.7706–0.8974 (n = 7)	1.8330–3.2644 (n = 7)
MMR	0.7098–0.7152 (n = 7)	17.86–18.65 (n = 3)	15.40–15.65 (n = 3)	0.8381–0.8634 (n = 3)	2.0629–2.0856 (n = 3)

Metamorphic blue sapphires have Sr isotopic compositions ranging from  $^{87}\text{Sr}/^{86}\text{Sr} = 0.7066 \pm 0.0020$  to  $^{87}\text{Sr}/^{86}\text{Sr} = 0.7316 \pm 0.0008$ . Among the different localities, Ilakaka, MDG has blue sapphires with the most radiogenic Sr isotopic composition (median  $^{87}\text{Sr}/^{86}\text{Sr} \sim 0.7206$ ), followed by Sri Lanka and Myanmar with median  $^{87}\text{Sr}/^{86}\text{Sr} \sim 0.7141$  and  $^{87}\text{Sr}/^{86}\text{Sr} \sim 0.7109$ , respectively (Figure 7d, Table 4). Only two blue sapphires from Andrebabe, MDG were analyzed, and represent the most unradiogenic suite with Sr isotopic ratios of  $0.7066 \pm 0.0020$  and  $0.7087 \pm 0.0024$ . For one blue sapphire from Myanmar (sample 0098), two Sr isotope analyses were carried out, giving two different  $^{87}\text{Sr}/^{86}\text{Sr}$  ratios:  $^{87}\text{Sr}/^{86}\text{Sr} = 0.7152 \pm 0.0008$  and  $^{87}\text{Sr}/^{86}\text{Sr} = 0.7130 \pm 0.0010$ .

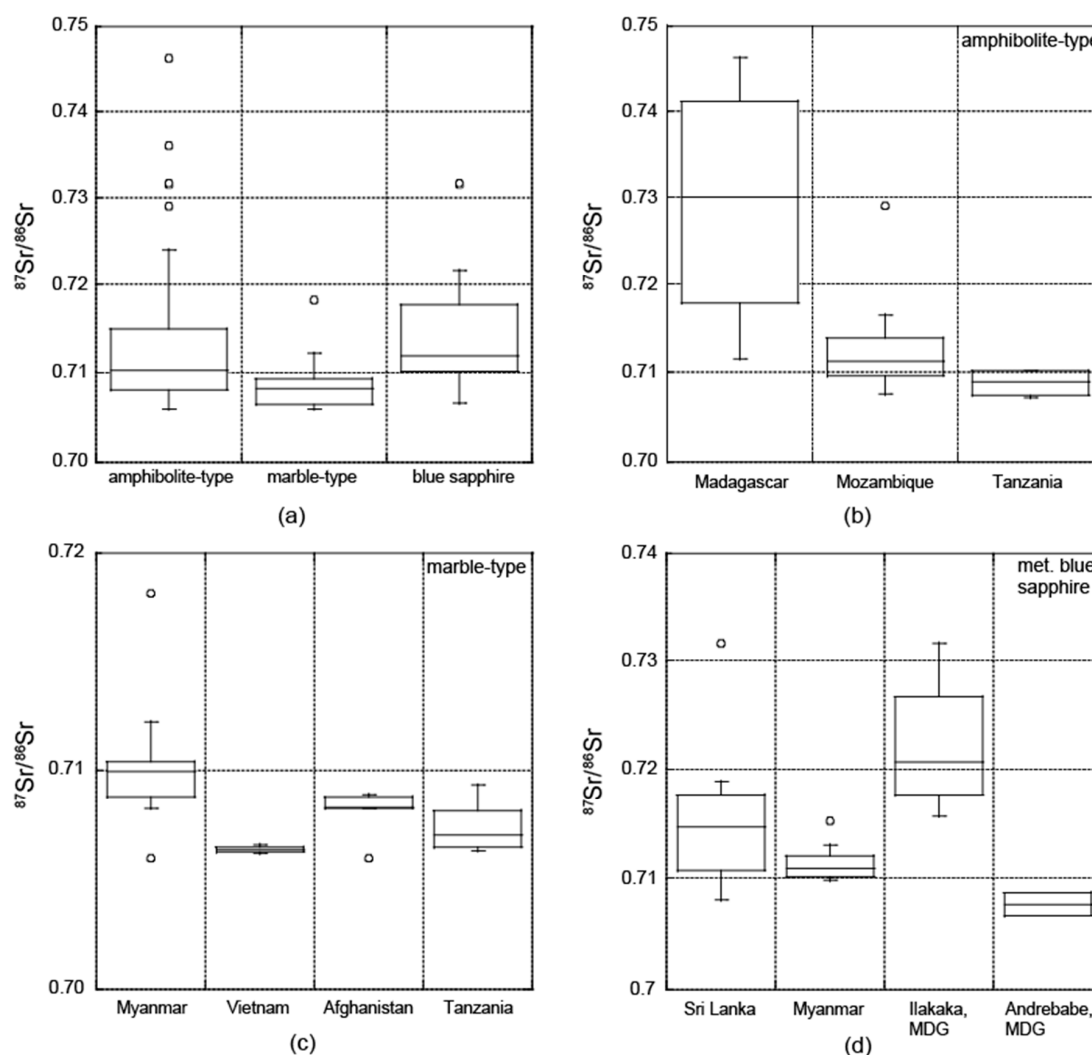


**Figure 7.** Box and whisker plots displaying  $^{87}\text{Sr}/^{86}\text{Sr}$  isotopic compositions of gem corundum from (a) the three different deposit groups, (b) the amphibolite-type ruby localities, (c) the marble-type ruby localities, and (d) the localities of metamorphic blue sapphire measured in this study. Individual data points are outliers whose value is either greater than  $\text{UQ} + 1.5 \times \text{IQD}$  or less than  $\text{LQ} - 1.5 \times \text{IQD}$  (where  $\text{UQ}$  = upper quartile,  $\text{LQ}$  = lower quartile, and  $\text{IQD}$  = inter quartile distance).

### 3.2.2. Pb Isotopic Composition

The relative variations in Pb isotopic compositions in corundum of the different groups are minor (Table 4, Figure 8a–d); the amphibolite-type rubies have slightly more unradiogenic compositions (median  $^{206}\text{Pb}/^{204}\text{Pb} \sim 17.93$ , median  $^{207}\text{Pb}/^{204}\text{Pb} \sim 15.58$ , median  $^{207}\text{Pb}/^{206}\text{Pb} \sim 0.8655$ , and median  $^{208}\text{Pb}/^{206}\text{Pb} \sim 2.1290$ ) than the marble-type rubies (median  $^{206}\text{Pb}/^{204}\text{Pb} \sim 18.63$ , median  $^{207}\text{Pb}/^{204}\text{Pb} \sim 15.61$ , median  $^{207}\text{Pb}/^{206}\text{Pb} \sim 0.8308$ , and median  $^{208}\text{Pb}/^{206}\text{Pb} \sim 2.0483$ ) and the metamorphic blue sapphires (median  $^{206}\text{Pb}/^{204}\text{Pb} \sim 18.50$ , median  $^{207}\text{Pb}/^{204}\text{Pb} \sim 15.58$ , median  $^{207}\text{Pb}/^{206}\text{Pb} \sim 0.8436$ , and median  $^{208}\text{Pb}/^{206}\text{Pb} \sim 2.0851$ ).

Among the different localities of amphibolite-type ruby, Pb isotopic ratios in samples from Zahamena, MDG span a wide range (e.g.,  $^{207}\text{Pb}/^{206}\text{Pb} = 0.6488 \pm 0.0003$  to  $0.9539 \pm 0.0005$ , Figure 9a), while the ranges for samples from Mozambique and Winza, TZA are much more narrow,  $^{207}\text{Pb}/^{206}\text{Pb} = 0.8305 \pm 0.0026$  to  $0.8655 \pm 0.0016$  and  $^{207}\text{Pb}/^{206}\text{Pb} = 0.8880 \pm 0.0003$  to  $0.9223 \pm 0.0002$ , respectively. For one ruby (sample moz2\_6), two Pb isotope analyses were carried out, giving two different  $^{207}\text{Pb}/^{206}\text{Pb}$  ratios,  $0.8655 \pm 0.0016$  and  $0.8305 \pm 0.0026$ .

Pb isotopic ratios of rubies from different marble-type localities overlap significantly, with median  $^{207}\text{Pb}/^{206}\text{Pb}$  values of  $\sim 0.8280$ ,  $\sim 0.8400$ ,  $\sim 0.8489$ , and  $\sim 0.8328$  for rubies from Myanmar; Vietnam; Afghanistan; and Morogoro, TZA, respectively (Figure 9b). Sample 5202 from Morogoro, TZA is much more radiogenic ( $^{207}\text{Pb}/^{206}\text{Pb} = 0.4615 \pm 0.0002$ ) than any other sample in this group, resulting in a wide range of Pb isotopic compositions for this locality.

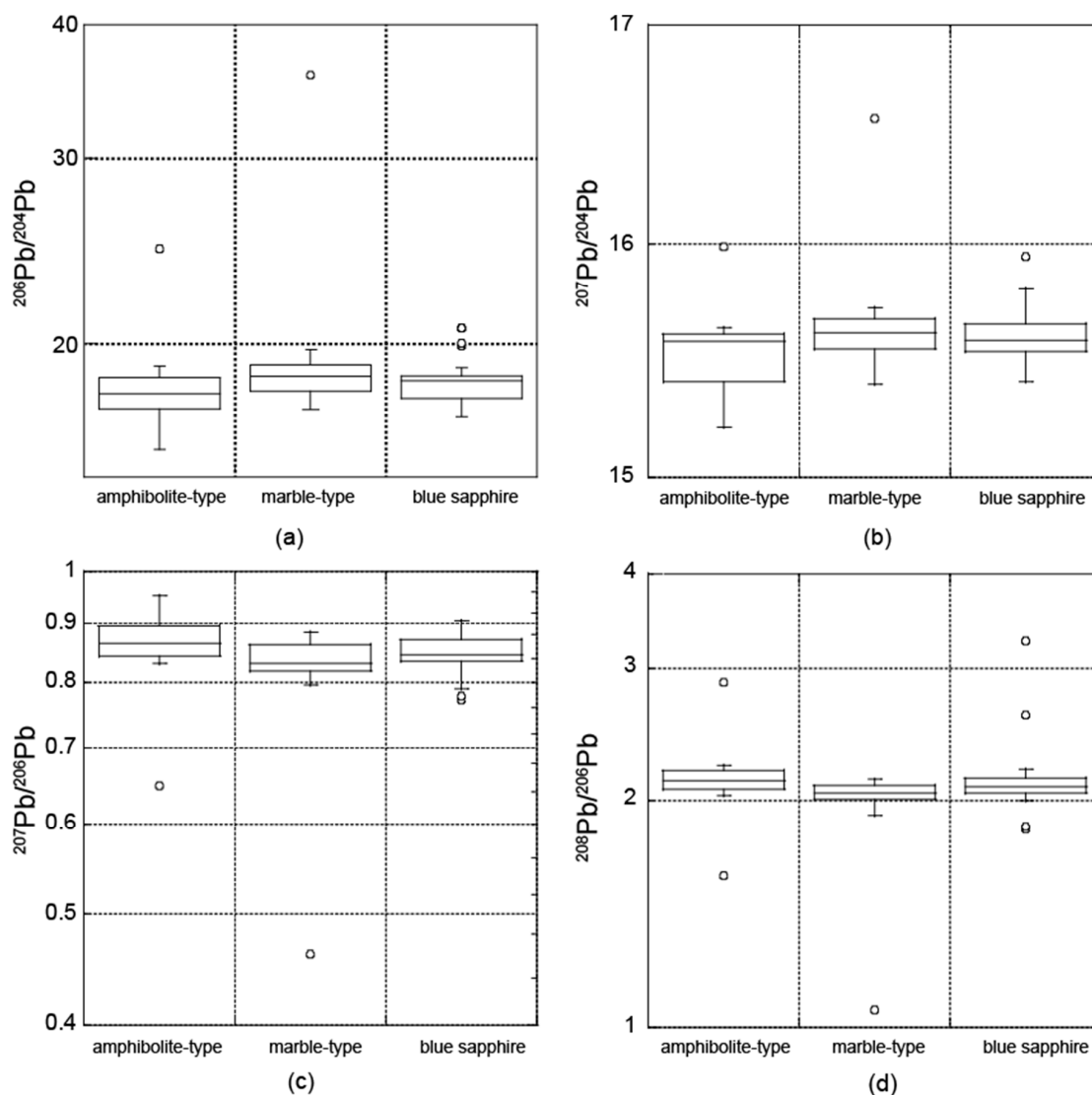


**Figure 8.** Box and whisker plots displaying (a)  $^{206}\text{Pb}/^{204}\text{Pb}$ , (b)  $^{207}\text{Pb}/^{204}\text{Pb}$ , (c)  $^{207}\text{Pb}/^{206}\text{Pb}$ , and (d)  $^{208}\text{Pb}/^{206}\text{Pb}$  isotopic compositions of gem corundum from the three different deposit groups measured in this study. Individual data points are outliers whose value is either greater than  $\text{UQ} + 1.5 \times \text{IQD}$  or less than  $\text{LQ} - 1.5 \times \text{IQD}$ .

Similar to the amphibolite-type and marble-type rubies, Pb isotopic ratios of metamorphic blue sapphires from different localities overlap (Figure 9). Samples from Andrebabe, MDG have the most unradiogenic Pb isotope ratios (e.g., median  $^{207}\text{Pb}/^{206}\text{Pb} \sim 0.8722$ ), followed by Myanmar with median  $^{207}\text{Pb}/^{206}\text{Pb} \sim 0.8574$ . Blue sapphires from Sri Lanka and Ilakaka, MDG are the most radiogenic with  $^{207}\text{Pb}/^{206}\text{Pb}$  median values of  $\sim 0.8384$  and  $\sim 0.8436$ , respectively.

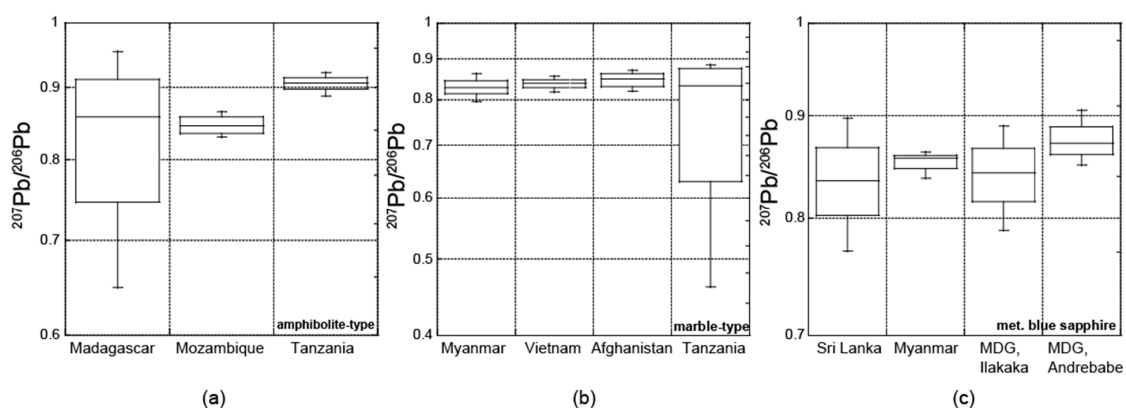


**Figure 9.** Box and whisker plots displaying  $^{207}\text{Pb}/^{206}\text{Pb}$  isotopic compositions of gem corundum from (a) the amphibolite-type ruby localities, (b) the marble-type ruby localities, and (c) the localities of metamorphic blue sapphire measured in this study.

No correlations between Sr and Pb isotopic compositions are apparent for any of the sample suites analysed in this study (Figure 10).

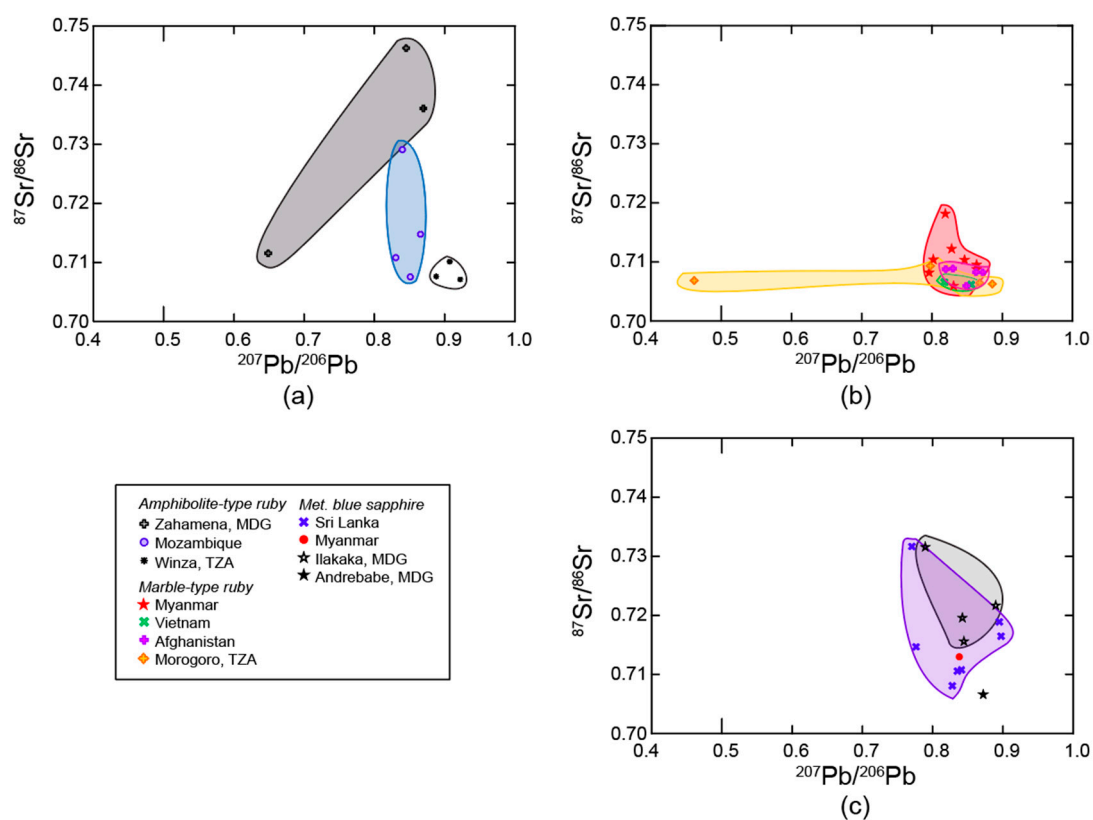


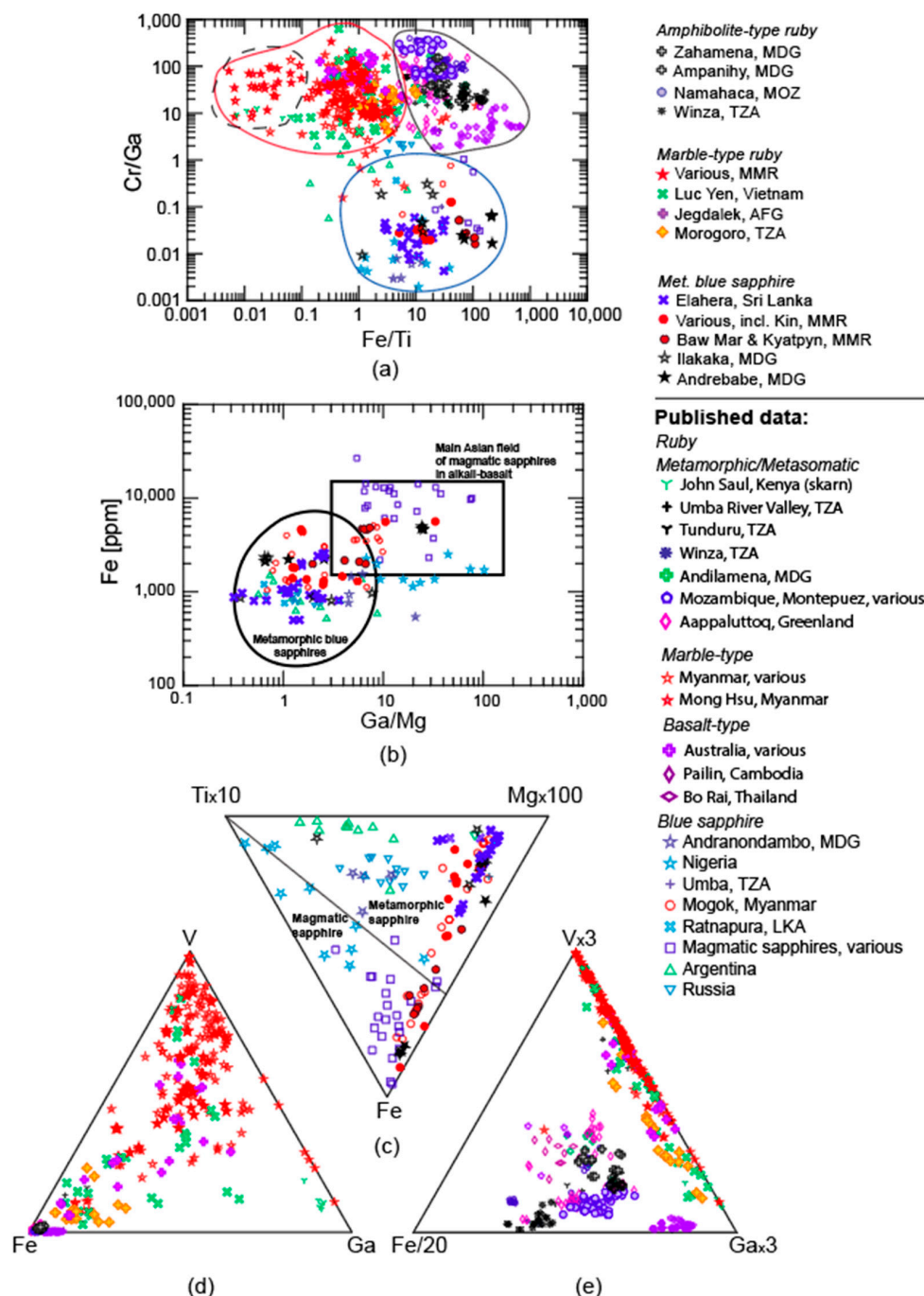
**Figure 10.**  $^{87}\text{Sr}/^{86}\text{Sr}$  vs.  $^{207}\text{Pb}/^{206}\text{Pb}$  ratios of (a) amphibolite-type rubies, (b) marble-type rubies, and (c) metamorphic blue sapphires measured in this study. Analytical uncertainties are less than the size of the plot symbols. Color of the fields correspond to the color of the symbols.

## 4. Discussion

### 4.1. Trace Elements

Quantitative data for the most commonly observed elements in ruby and sapphire—Fe, Cr, Ti, V, and Ga—have been used by many authors (e.g., [8–10,15,33,59,60]) in attempts to determine gem

corundum provenance. Figure 11 comprises a number of existing discrimination schemes, showing how our data compare with previously published data from the same localities. A number of classical and non-classical deposits are also plotted to place our data into worldwide context. A commonly used diagram is a logarithmic plot of wt% values  $\text{Cr}_2\text{O}_3/\text{Ga}_2\text{O}_3$  versus  $\text{Fe}_2\text{O}_3/\text{TiO}_2$  (e.g., [8,9,61]).



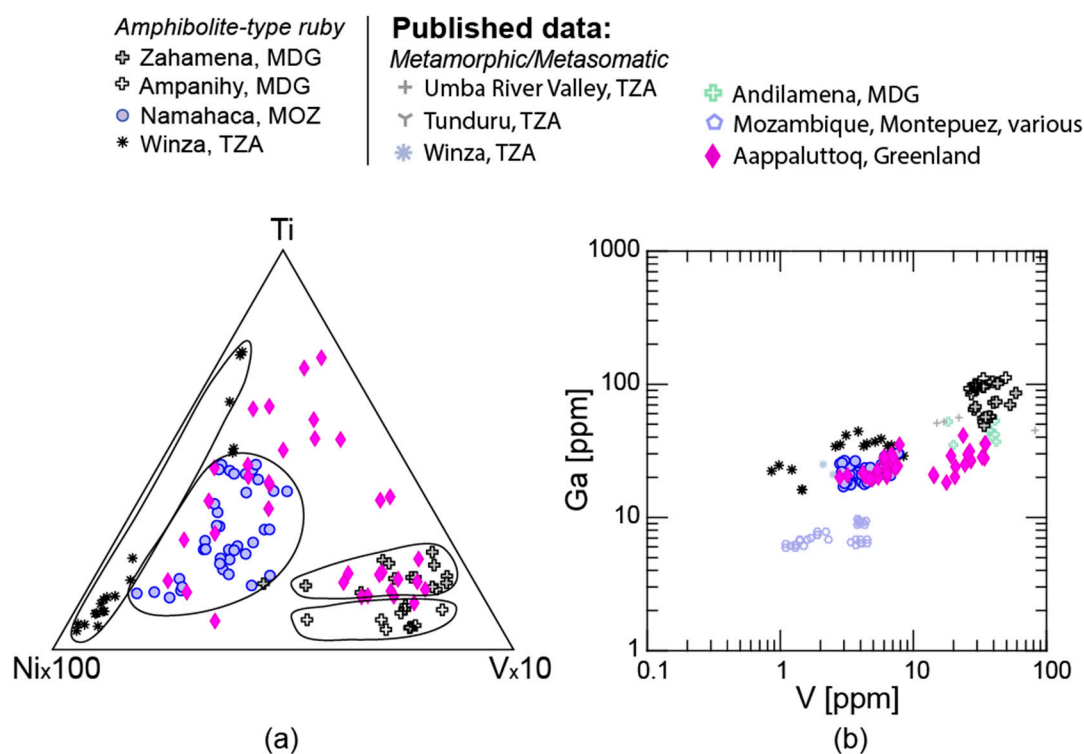
**Figure 11.** (a) Plot of Cr/Ga (ppm) versus Fe/Ti (ppm) (modified from [8]); fields are red = marble-type, black/dashed = Mong Hsu ruby [62], black = high Fe, and blue = blue sapphires. (b) Fe (ppm) versus Ga/Mg (ppm) (after [10]); (c) Mg × 100–Fe–Ti × 10 ternary plot modified after [10]; and (d) Fe–V–Ga ternary plot (after [15]), and (e) Fe/20–V × 3–Ga × 3 (after [28]) in gem corundum analyzed in this study. All data plotted are laser ablation inductively coupled plasma mass spectrometry (LA-ICP-MS) values. Additional data from [10,23,25,33,42,43,59,60,62–69].

Figure 11a is a plot of Cr/Ga versus Fe/Ti for the gem corundum suites analyzed in this study. Published datasets used for comparisons are exclusively LA-ICP-MS data, excluding electron microprobe (EMPA) data sets, because it has been shown that data derived from the different methods vary systematically for several elements [33]. In such a plot, marble-type rubies have  $\text{Cr/Ga} > 1$  and  $\text{Fe/Ti} < 6$ , while high-Fe rubies, including amphibolite-type and basalt-type ruby, have  $\text{Cr/Ga} > 1$  and  $\text{Fe/Ti} > 6$ . Blue sapphires, with measurable Cr, have  $\text{Cr/Ga} < 1$  and  $\text{Fe/Ti} > 1$ . Exceptions are two non-classical deposits, a suite of alluvial sapphires from Argentina [68], which have  $\text{Cr/Ga}$  of up to  $\sim 4$  and  $\text{Fe/Ti} > 0.1$ , and a suite from the Ural mountains in Russia [67], with  $\text{Cr/Ga} \sim 1\text{--}3$ . High-Fe rubies, marble-type rubies, and blue sapphires thus fall into discrete fields with only minor overlap along the boundaries. However, different localities within the different deposit type groups overlap significantly. Blue sapphires, with the exception of the above-mentioned suites, overlap regardless of origin (metamorphic versus magmatic) and locality. Diagrams of Fe versus Ga/Mg and  $\text{Mg} \times 100\text{-Fe-Ti} \times 10$ , first introduced by [10], can be used to separate blue sapphires based on their geological origin. On such plots, the majority of our data of different metamorphic blue sapphire suites fall into the fields defined for metamorphic blue sapphires (Figure 11b,c). However, we note that several of our samples from Myanmar, specifically from the Baw Mar and Kyatpyn mines, and Andrebabe, MDG, fall into the “magmatic sapphire” field. In addition, a suite of blue sapphires from the northern part of the Baw Mar mine also plots as magmatic, despite the fact that these samples were classified as metamorphic based on standard gemological techniques, including inclusion studies and UV/vis spectroscopy [43]. On the basis of the geology at the mine site, these sapphires likely formed either directly in syenitic pegmatites or through the interaction of such pegmatites with surrounding marbles and/or gneisses [43]. In other words, trace element and gemological characteristics suggest that subgroups of sapphires classified as metamorphic formed in a metamorphic environment, but from magmatic rocks. As such, their trace elements reflect the magmatic nature of their host rock, while UV/vis spectroscopy and inclusions speak to their metamorphic origin. This illustrates that existing classification schemes for blue sapphire cannot account for the complex geological processes that form blue sapphires. However, both the Fe versus Ga/Mg and  $\text{Mg} \times 100\text{-Fe-Ti} \times 10$  classification diagrams are useful in separating syenite-related metamorphic sapphire from Myanmar and Andrebabe, MDG, from those from Sri Lanka and Ilakaka, MDG. Within the respective fields, however, these populations overlap.

Among the marble-type rubies, only those from Mong Hsu, MMR [62], which is located about 250 km southeast of Mogok, are clearly distinguishable in Figure 11a, with much lower Fe/Ti values than those from the other localities. Rubies from Afghanistan analysed in this study have higher Cr/Ga than those from Morogoro, TZA, however, both localities overlap with rubies from Myanmar and Vietnam. The overlap is somewhat less complete among the amphibolite-type rubies, with those from Winza, TZA, and Ampanihy, MDG, analyzed in this study plotting at slightly lower Cr/Ga and higher Fe/Ti than those from Mozambique, the Andilamena area in Madagascar, Greenland, and basalt-type rubies from Cambodia and Thailand. However, only the basalt-type population from the New England Gem field, Australia, displaying relatively high Fe/Ti and low Cr/Ga indicative of igneous origin [8], does not overlap with other deposits. This deposit is thought to have experienced magmatic-metasomatic inputs in its genesis [66]. When plotting the same data on a ternary diagram depicting Fe–V–Ga concentrations (Figure 11d) after [15], high-Fe rubies all plot at the Fe-apex, while the low-Fe marble-type rubies show a wider distribution. Myanmar rubies plot at higher V; those from Morogoro, TZA, plot close to the Fe-apex; and rubies from Afghanistan and Vietnam overlap both suites. While basalt-type rubies overlap with amphibolite-type ruby here, they are easily separated from other high-Fe rubies using Mg [5]. Smith et al. [28] modified the Fe–V–Ga ternary diagram to  $\text{Fe}/20\text{-V} \times 3\text{-Ga} \times 3$  to provide more resolution in the Fe-apex area of the plot (Figure 11e). This approach allows the distinction of the basalt-hosted rubies from most rubies of metasomatic and metamorphic origin, but there is still significant overlap for the various localities. Only rubies from Winza, TZA, show minimal overlap.

The overlap of samples from the different localities of both ruby groups examined here, as well as that among metamorphic blue sapphires, in commonly-used discrimination schemes, illustrates that, while they are useful in distinguishing rubies of different geological deposit types, they are not very effective in distinguishing between different localities of the same deposit type.

The broader spectrum of quantitative trace element data we were able to obtain using the ablation and measurement parameters detailed in Section 2.2.1 now makes it possible to evaluate the use of additional elements as provenance discriminators that have not been yet measured consistently. Amphibolite-type rubies in particular show a much broader spectrum of trace elements consistently >LOQ, while such additional elements are fairly limited for the marble-type rubies. The main reason for this is very likely the (on average) higher clarity of the marble-hosted rubies analysed in this study (Figure A2). This suggests that the potential of using such low abundance elements is fairly limited, at least with the current sensitivity of the LA-ICP-MS method, because the main goal of developing a geochemical fingerprint is the determination of provenance for high-quality gemstones. However, the elements Ni, Zn, and Pb are consistently > LOQ for all corundum analysed in this study, regardless of geologic origin or clarity, and were thus included in the discrimination evaluation. Of these elements, Pb has proven to be ineffective as discriminator of geographic locality, at least for the deposit types and localities analysed in this study as contents between the analysed suites overlap significantly. Ni, however, shows good discriminatory power for the separation of different localities of amphibolite-type ruby (Figure 12a), and, in conjunction with Ti and V, defines discrete fields for rubies from Winza, TZA, Mozambique, Zahamena, MDG, and Ampanihy, MDG. Rubies from Greenland, however, have a wide range of Ni, Ti, and V contents, resulting in significant overlap on a Ni  $\times$  100-Ti-V  $\times$  10 plot (Figure 12a). Some of this overlap can be resolved by further plotting the data on a binary Ga versus V plot (Figure 12b), thus effectively separating the Greenland rubies from those from Madagascar; minor overlap of Mozambique and Greenland persists, however.



**Figure 12.** (a) Ternary diagram of Ni  $\times$  100-Ti-V  $\times$  10 for amphibolite-type rubies analyzed using LA-ICP-MS in this study. Greenland data are taken from [12]. (b) Binary plot of Ga (ppm) versus V (ppm) abundances in amphibolite-type rubies analyzed in this study. Additional data from [23,25,59].

On the Ga versus V plot, rubies from the Andilamena region in Madagascar [59] plot at slightly lower Ga values than those analyzed in this study. More notably, rubies from Mozambique analyzed by [23] have significantly lower Ga contents than rubies from Mozambique in this study. Both these studies used matrix-matched synthetic corundum standards as calibration materials, while in this study, NIST612 was used, resulting in more accurate analyses for their data. These differences emphasize the importance of using matrix-matched standards for accurate LA-ICP-MS analyses, and also illustrate that, for effective comparative studies, the same LA-ICP-MS system and reference materials should be used.

For the discrimination of different localities among marble-type rubies, none of the additional trace elements obtained in this study add further discriminatory power. Instead, a combination of the most abundant trace elements in corundum delivers the best results (Figure 13). A binary plot of V versus Cr roughly divides rubies from Myanmar; Morogoro, TZA; and Afghanistan into separate fields with only minor overlap (Figure 13a), while a binary plot of Fe versus V clearly separates the Myanmar rubies analyzed in this study from those from Morogoro, TZA (Figure 13b). Ternary diagrams of  $\text{Fe/Mg} \times 2\text{-Cr/Ti-V}/10$  and  $\text{V-Cr}/10\text{-Ti}$  archive similarly passable separations of Myanmar; Morogoro, TZA; and Afghanistan rubies (Figure 13c,d). However, rubies from Vietnam have very variable trace element abundances and overlap with all other marble-type localities analysed in this study. Previously published data of Myanmar rubies [33,62] agree reasonably well with data from this study, however, the data presented here are more variable.

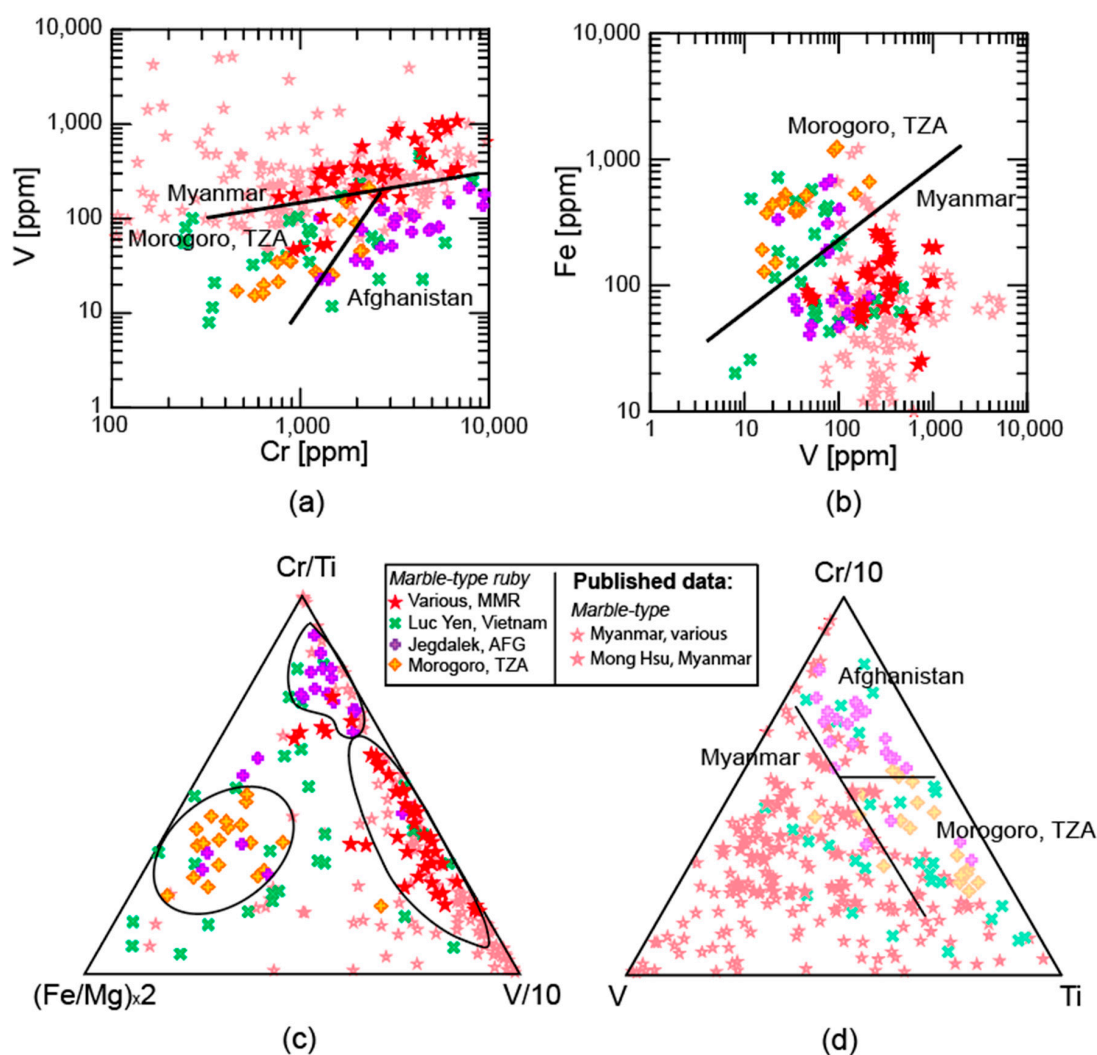


**Figure 13.** (a) Binary plot of V (ppm) versus Cr (ppm), (b) binary plot of Fe (ppm) versus V (ppm), (c) ternary diagram of  $Fe/Mg \times 2$ - $Cr/Ti$ - $V/10$ , and (d) ternary diagram of  $V$ - $Cr/10$ - $Ti$  for marble-type rubies analyzed using LA-ICP-MS in this study. Fields are drawn by eye. Additional data from [33,62].

As for marble-type ruby, none of the additional elements obtained in this study added obvious further discriminatory power for the separation of different localities of metamorphic blue sapphire. However, Cr, which is often reported close to or below the LOD for samples from the localities studied here [10,70], is consistently above LOQ and shows potential as an additional discriminatory element. A binary plot of Mg versus V separates sapphires from Myanmar and Andrebabe, MDG, from sapphires from Sri Lanka and Ilakaka, MDG. In addition, syenite-related metamorphic sapphires have lower Mg (<20 ppm) and V (<4 ppm). A bivariate plot of V versus  $Cr \times Ti$  separates Sri Lanka and Ilakaka, MDG, sapphires with only minor overlap (Figure 14). Myanmar and Andrebabe, MDG, with magmatic trace element signatures, have low  $Cr \times Ti$ . Using a bivariate diagram of V versus  $Ga/Ti$ , the Andrebabe, MDG sapphires can be separated from both the Myanmar and the overlapping Sri Lanka and Ilakaka, MDG sapphires (Figure 14c). Previously published data for sapphires from Andranondambo, MDG [59] show significant overlap with sapphires from Sri Lanka and Ilakaka, MDG. Trace element compositions previously published for Myanmar sapphires [42,43] are more variable than those analyzed in this study. Metamorphic sapphires from Russia [67] and Argentina [68] are easily distinguished from the other localities by their high  $Cr \times Ti$  and low and high V contents, respectively (Figure 14b).

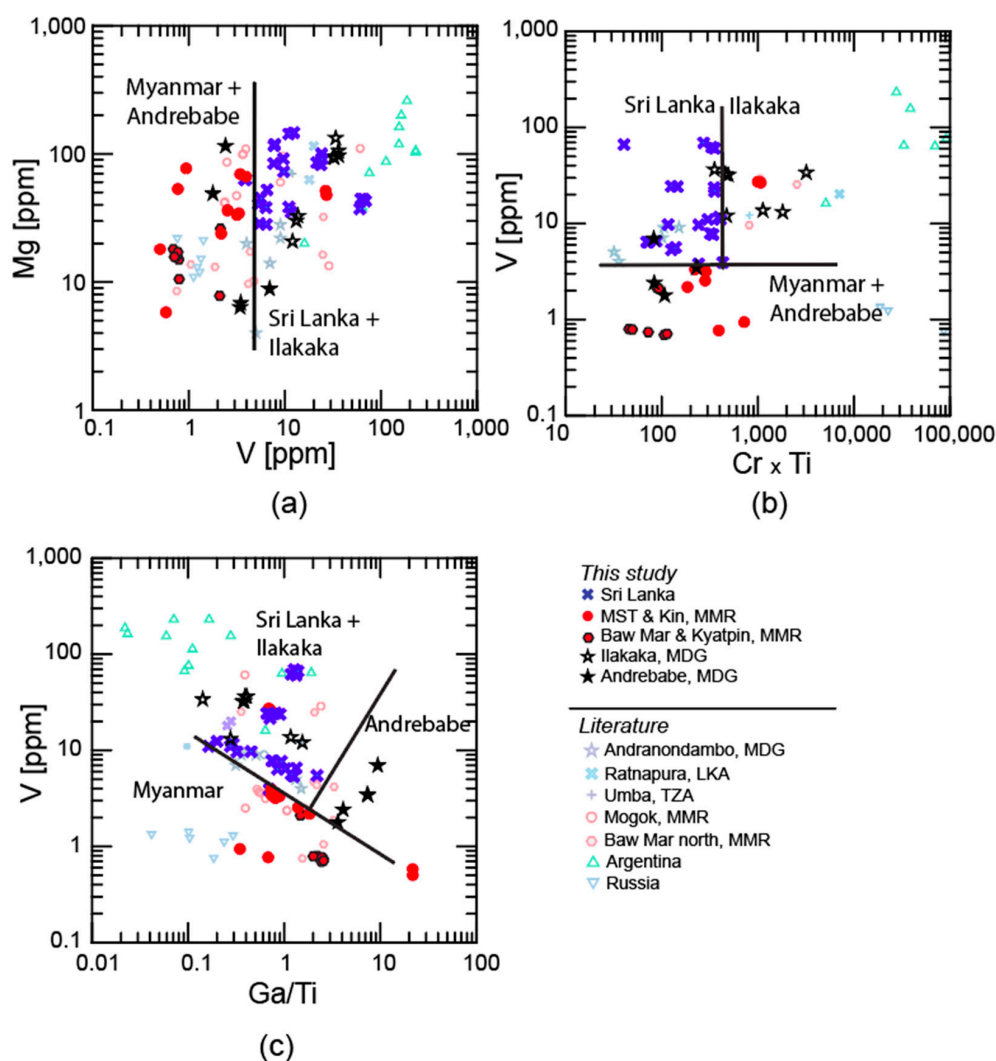


**Figure 14.** Binary plots of (a) Mg (ppm) versus V (ppm), (b) V (ppm) versus Cr  $\times$  Ti (ppm), and (c) V versus Ga/Ti for metamorphic blue sapphires analyzed using LA-ICP-MS in this study. Fields are drawn by eye. Additional data from [10,42,43,59].

The results show that distinguishing between blue sapphires from Sri Lanka and Myanmar using trace elements is easily accomplished. Sapphires from Madagascar, however, show extensive chemical overlap with sapphires from other localities, which can be somewhat well-resolved for the small number of samples analyzed here. Madagascar has a vast number of ruby and sapphire deposits that are most often secondary deposits with stones that have formed in a variety of different geological settings [27]. As such, they are not only characterized by very variable trace element characteristics, but also a strong gemological diversity, and are known to overlap (sometimes significantly) with metamorphic sapphires from all other major sources [4].

Multivariate statistical analysis, including principal component analysis (PCA) and linear discriminant analysis (LDA), is a tool to identify patterns and relationships between multiple variables simultaneously and can, potentially, increase the reliability of origin determination as well as detect elements with potential discriminatory power. Both PCA [59,71] and LDA [59] have been successfully applied to rubies and sapphires of different geological deposit types; here, we apply both approaches to visualise the compositional differences for samples of the same geological type from different localities. Calculation of robust quantitative discriminants in this study is restricted by the modest

population sizes, so we use PCA and LDA to qualitatively determine which elements might have discriminatory value.

To this end, we applied LDA to our online LA-ICP-MS dataset, using the software R (for details on R runstreams see Supplementary Material S4). LDA is a dimension reduction technique that defines linear discriminants that maximize the “distance” between the means of pre-defined classes. Data for rubies from Greenland [12] were included in the calculations for the amphibolite-type group, because they were collected on the same system using the same ablation and measurement conditions. LDA solutions are derived using the full dataset as calibration data, and the classification error (CE) of the method is determined by testing the calibration data on the method by the following formula:

$$\text{CE} = \text{number of incorrect classifications} / \text{total number of samples} \times 100\% \quad (1)$$

As the CE for the calibration data of the method it calibrated will result in an overly optimistic assessment of classification success or failure, solutions are assigned a method uncertainty by K-fold cross validation. This is conducted by subdividing the sample sets into five random folds with 80% of the data classified as “calibration” data, and the remaining 20% as “validation” data. An LDA solution is derived using the calibration set of a single fold, and tested with its respective validation dataset. This is conducted upon all five folds, and the calculated error rates for the folds are then averaged and taken as the method uncertainty.

For the amphibolite-type deposits, LDA was applied iteratively to the datasets using combinations of chemical variables; through this process, we narrowed the number of most useful variables down to four—V, Fe, Mg, and Ni—by excluding those elements that only reproduce existing discrimination power of others. This result confirms the potential of Ni as an element with discriminatory power for the amphibolite-type deposits evaluated in this study. To assess its influence, an LDA solution using only V, Fe, and Mg was applied (Figure 15a). This solution results in some overlap of rubies from Ampanihy, MDG; Winza, TZA; and Greenland, as well as some overlap of rubies from Greenland with rubies from Mozambique, similar to that observed using a ternary diagram of  $\text{Ni} \times 100\text{-Ti-V} \times 10$  (Figure 12a). By adding Ni to the solution, only the overlap of Greenland with Mozambique remains (Figure 15b), and the CE is minimized at ~13.7%. The average K-fold ( $n = 5$  folds) cross-validation error of  $17.33 \pm 11.93$  ( $2\sigma$ ) is identical for both solutions (Supplementary Material S5).

For marble-type deposits, an LDA solution using seven elements—V, Fe, Ga, Mg, Ti, Cr, and Zr—gives the best discrimination for the different localities studied here. While Zr shows no obvious discriminatory power in elemental plots, it influenced the LDA calculations positively. Bivariate plots of the linear discriminants (LDs) show a good separation of Morogoro, TZA and Myanmar (Figure 15c,d), similar to the discrimination achieved by plotting elemental abundances against each other (e.g., Figure 13b,c). In addition, the LDA solution results in a better discrimination of Vietnam rubies from Morogoro, TZA (Figure 15c) and from Afghanistan rubies (Figure 15d), which otherwise overlap significantly in the graphical bivariate discrimination schemes using elemental abundances (Figure 13). However, the chemical overlap is still significant with a CE of ~21% and a similar average K-fold ( $n = 5$  folds) cross-validation error of  $19.09 \pm 11.85$  ( $2\sigma$ ).

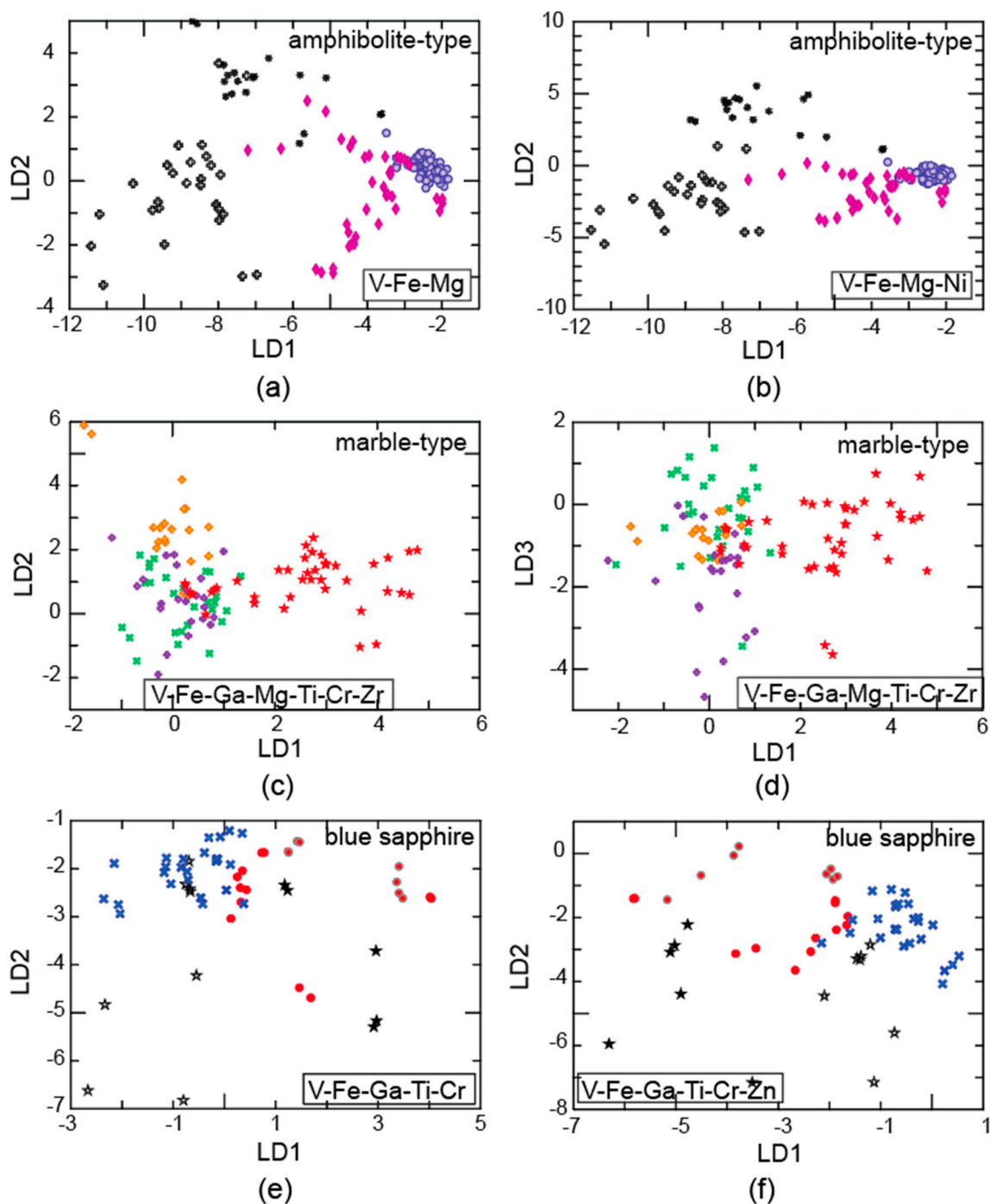


**Figure 15.** Linear discriminant analysis (LDA) solution for (a), (b) amphibolite-type rubies; (c), (d) marble-type rubies; and (e), (f) metamorphic blue sapphires. Elements used in method calibration are inset on each figure. Symbols as in Figure 11.

For application of LDA to the metamorphic blue sapphires, the Myanmar sapphires were separated into two groups based on the inference that they have discrete geological origins, resulting in five overall groups including the other locations. The best results were obtained using the six elements V, Fe, Ga, Ti, Cr, and Zn. Because Zn shows no obvious discriminatory power in elemental plots, an LDA solution using only V, Fe, Ga, Ti, and Cr was also applied. The results show a clear improvement with the inclusion of Zn, reducing the overlap between sapphires from Sri Lanka and Ilakaka, MDG (Figure 15e,f). The one obvious outlier of the Mogok Stone Tract (MST) & Kin, MMR group behaves similar in the

discrimination schemes using elemental abundances (Figure 14), reflecting a syenite-related origin. Whether this indicates that syenite-related samples are also found at the Kin mine or if the sample was mislabeled is unclear. The CE for the LDA solution calibrated on the elements V, Fe, Ga, Ti, and Cr is ~27%, and ~18.6% for the solution calibrated on the elements V, Fe, Ga, Ti, Cr, and Zn, showing a clear improvement of the classification through the addition of Zn. No K-fold cross-validated error is calculated here owing to the small sample sets, which result in erratic calculated error rates, being prone to over- or underestimation of the true success or failures of the LDA methods. This is indicated by the large standard deviation of the average cross-validation error of the amphibolite-type group, which is the largest dataset in this study.

#### Comparison of Online and Offline Laser Ablation Approaches

Aside from a small number of elements that substitute for  $Al^{3+}$  in the crystal structure (e.g., Mg, Cr, Fe, V, Ti, and Ga), trace elements in gem corundum are present as mineral inclusions or as constituents in fractures, and their absolute trace element abundances are primarily a function of impurity density [12]. Therefore, the larger sampling volumes of the offline ablation approach result in more varied trace element characteristics that correspond to the presence of nano- to micrometer-sized mineral and fluid inclusions characteristic of the ruby or sapphire forming environment. Such variations are evident in the differences in  $Ta/Nb_N$ ,  $U/Pb_N$ ,  $Th/U_N$ , and  $Zr/Hf_N$  ratios between online- and offline-ablated material, with the former showing variations for different localities and the latter showing complete overlap for all localities and deposit types (Figure A1a–l). Some of the trace element characteristics of the offline-ablated material show differences that could be utilized for geographic origin determination of different localities of similar deposit types, including, for example, the  $Eu/Eu^* > 1$  of Mozambique rubies (Figure 4a), and the  $Sr/Sr^* < 1$  for Myanmar rubies. Some suites are also characterized by the absence or certain trace elements, Sr, for example, is below < LOQ in all rubies from Zahamena, MDG, and Cs in sapphires from Myanmar and Andrebabe, MDG. Most of these trace element characteristics, however, are specific to a certain deposit, and as such, cannot be applied universally. In addition, the number of samples ablated offline is small, and some characteristics observed may well be a result of low sample numbers. Owing to the small sample set sizes, we do not apply LDA to explore the data for useful chemical variables, as the derived discriminants may be skewed by the—potentially—non-representative datasets. Given the chemical variation within this modest sample set, outliers weighted more strongly on the solution than they would for a larger dataset. Instead, as a preliminary check, we applied PCA to the offline-ablated trace element datasets to identify possible chemical discriminants for provenance, associated with chemical variance. However, no clear discrimination is apparent in principal component space for the present datasets. Therefore, while some of the trace element characteristics observed may provide additional information valuable for provenance, at this time, they have little potential for the development of a robust geochemical fingerprint of provenance for gem corundum. As more data are acquired, the application of LDA and PCA to variable selection and class discrimination may be more appropriate.

#### 4.2. Radiogenic Isotopes

As demonstrated in Section 4.1, geographic origin determination using trace elements is useful in distinguishing between deposits of different geological deposit types, however, to distinguish between deposits of similar geological type, but different locality is challenging. Similar challenges are faced when using classical gemological techniques [4]. In this study, we obtained Sr and Pb isotopic compositions for ruby and blue sapphire from a variety of different localities of three different geological groups to explore the potential of using isotopic tracers to constrain geographical origin. We evaluated the usefulness of all combinations of isotopic ratios and trace elements, and a selection of the most useful discriminatory plots is shown in Figure 16.

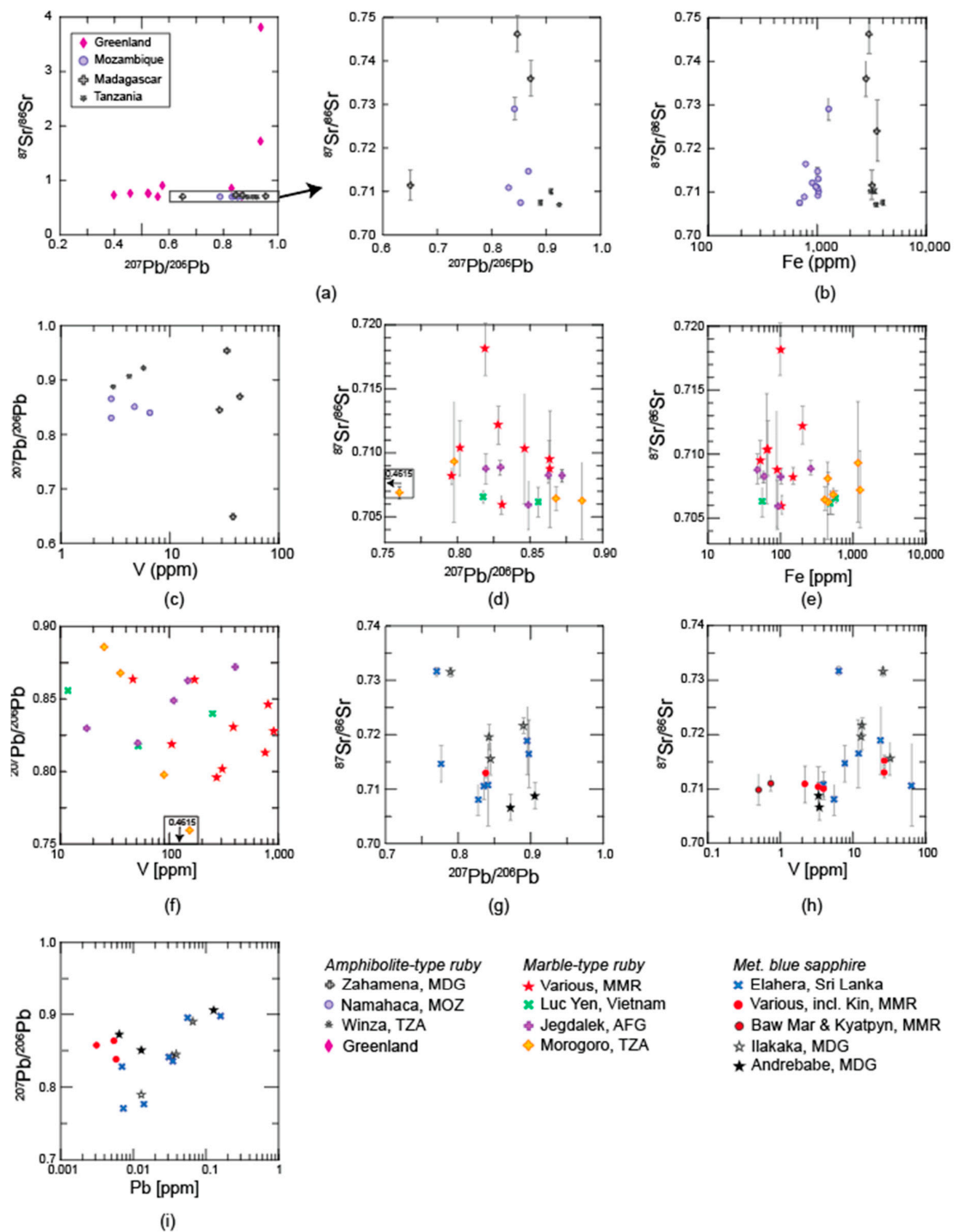


**Figure 16.** Radiogenic isotope characteristics of rubies and blue sapphires analyzed in this study. (a)  $^{87}\text{Sr}/^{86}\text{Sr}$  versus  $^{207}\text{Pb}/^{206}\text{Pb}$ , (b)  $^{87}\text{Sr}/^{86}\text{Sr}$  versus Fe (ppm), and (c)  $^{207}\text{Pb}/^{206}\text{Pb}$  versus V (ppm) of amphibolite-type rubies. (d)  $^{87}\text{Sr}/^{86}\text{Sr}$  versus  $^{207}\text{Pb}/^{206}\text{Pb}$ , (e)  $^{87}\text{Sr}/^{86}\text{Sr}$  versus Fe (ppm), and (f)  $^{207}\text{Pb}/^{206}\text{Pb}$  versus V (ppm) of marble-type rubies. (g)  $^{87}\text{Sr}/^{86}\text{Sr}$  versus  $^{207}\text{Pb}/^{206}\text{Pb}$ , (h)  $^{87}\text{Sr}/^{86}\text{Sr}$  versus V (ppm), and (i)  $^{207}\text{Pb}/^{206}\text{Pb}$  versus Pb (ppm) of metamorphic blue sapphires. Where error bars are absent, uncertainties are smaller than the symbols.

The discrimination of rubies from different amphibolite-type deposits is fairly straight-forward using trace elements obtained via online LA-ICP-MS, however, some chemical overlap remains between rubies from Greenland with those from Mozambique (Figures 12 and 15a,b). This overlap can be resolved using both Sr and Pb isotopes, because Greenland rubies have been shown to be much more

radiogenic than rubies from Mozambique, spanning a wide range of compositions ([12], Figure 16a). It is clear that these very distinct differences in isotopic compositions are largely because of the vast difference in formation age for the Greenland and Mozambique ruby deposits (Pb-Pb = ~2686 Ma [12] and ~550 Ma [72], respectively).

Therefore, it is unsurprising that rubies from Zahamena, MDG and Winza, TZA that formed during the Pan-African orogeny (750–450 Ma) [20] have radiogenic isotope compositions more similar to those of Mozambique, with some minor overlap between the different localities (Figure 7b). Nevertheless, when plotting Sr and Pb isotopic compositions against each other or against trace elements, for example, Fe or V, the different localities fall into discrete fields (Figure 16a–c), demonstrating the usefulness of Sr and Pb isotope ratios for determining the geographic origin of different amphibolite-type deposits.

As shown in Section 3.2.2, the range in Sr isotopes of marble-hosted rubies is much narrower than those of the analysed suites of amphibolite-type ruby, and the overlap among the different localities of marble-type deposits is greater than that of amphibolite-type deposits (Figure 7c). While Myanmar and Afghanistan rubies tend to have more radiogenic Sr compositions than rubies from Vietnam or Morogoro, TZA, the overlap precludes any usefulness such trends might provide, even when combining Sr isotopic ratios with trace elements (e.g.,  $^{87}\text{Sr}/^{86}\text{Sr}$  versus Fe, Figure 16e). This overlap of the different localities is even more complete for the Pb isotopic compositions (Figures 9b and 16b).

Similar to the marble-type rubies, metamorphic blue sapphires from different localities show significant overlap. Myanmar and Andrebabe, MDG sapphires generally show less radiogenic isotopic ratios than those from Sri Lanka and Ilakaka, MDG. This could be because of differences in the geological formation of the different deposits and differences in the age and lithology of their source components. In the MST, gem corundum of multiple geological origins was found and is thought to have formed either in connection with intrusions of granitoid rocks (leucogranites and hornblende syenites; between 35 and 23 Ma [62,73]) or regional metamorphism (sillimanite-grade high-temperature metamorphism; from at least 43 to 29 Ma [74]) [20]. The Elahera deposit in Sri Lanka, on the other hand, is an exoskarn deposit formed by the interaction of pegmatitic fluids with dolomitic marble [75]. The Ilakaka deposit in Madagascar is a secondary deposit and carries a wide variety of different sapphires, likely derived from several distinct geological formations. The sources are thought to be multiple and associated with granulite-facies metamorphism [20]. To date, nothing is known about the geology of the Andrebabe deposit in Madagascar, however, the trace element characteristics indicate an association with magmatic rocks. Another explanation could be different formation ages, because sapphires from Myanmar are thought to have formed during the Cenozoic Himalayan orogeny (e.g., zircon U–Pb ~25 Ma for foliated syenite associated with sapphire mineralization [76]), while the sapphires from Sri Lanka and Madagascar formed during the Pan-African orogeny (750–450 Ma) [20,27]. The observed overlap, complete for Sri Lanka and Ilakaka, MDG sapphires, can only partly be resolved when plotting Sr or Pb isotopic ratios against trace elements (Figure 16g–i), and the use of Sr and Pb isotopic compositions for geographic origin determination has proven to be relatively ineffective. No PCA solution yielded positive results.

## 5. Conclusions

Using an LA-ICP-MS method that combines a large spot size (285  $\mu\text{m}$ ) with a high repetition rate (20 Hz), we obtain a broader spectrum of quantitative trace element data than that obtained with more conventional approaches (spot size ~50  $\mu\text{m}$ , repetition rate of 5–10 Hz; for example, [23,62]). This permits the determination of up to 26 elements at levels above the limit of quantification (LOQ) in some rubies and sapphires. Using elemental discrimination schemes and linear discriminant analysis (LDA), we have shown that elements other than the conventional Mg, Ti, V, Cr, Fe, and Ga—which can substitute for  $\text{Al}^{3+}$  in the corundum crystal lattice—have the potential to be of use in geographic origin determination. The discrimination of the different localities of amphibolite-type ruby analyzed in this study is improved using Ni. For marble-type ruby, LDA results show that adding Zr positively influences the discrimination of the different marble-type localities. For metamorphic blue sapphire,

the discrimination of corundum from the different localities analyzed in this study is improved by Zn concentrations. In addition, Cr, which is often below the LOD for blue sapphires from the localities analyzed in this study using conventional methods [10], positively impacts the discrimination. While the discrimination of the different localities of the three different deposit groups is fairly good using LDA, some population overlap persists, particularly among the marble-type rubies and blue sapphires. This is not surprising owing to the very similar geological conditions of formation. The larger spot size of the LA-ICP-MS method used here precludes it from use in gemological laboratories on precious stones; however, our results indicate directions of focus for future method development. Trace element characteristics of the offline-ablated material show some differences that could be utilized for geographic origin determination of different localities of similar deposit types; however, the majority of these are specific to a certain deposit and, as such, may not be applied universally. Sr and Pb isotope compositions, obtained using offline laser ablation sampling followed by TIMS, have only limited potential for geographic origin determination at this time. Measured  $^{87}\text{Sr}/^{86}\text{Sr}$  and Pb isotope ratios of rubies from different amphibolite-type deposits show distinct ranges and separate fields on bivariate plots that are positive indicators of discrimination. For marble-type rubies and metamorphic blue sapphires, however, different geographic origins overlap.

Overall, our results show that the discrimination of different geographic regions of similar geological deposit types using trace elements is fairly simple for amphibolite-type rubies, while it is much more challenging for marble-type rubies and metamorphic sapphires. As more data from these localities are acquired and analyzed, discriminants can be refined and developed further. However, adding additional localities might lead to more significant overlap. Similarly, radiogenic isotopes show discriminatory potential for amphibolite-type rubies, but not marble-type rubies or metamorphic blue sapphires, likely owing to significant isotopic variability in the different components that combine to form these gems. Our results re-emphasize both the promise of using combined isotopic and trace element fingerprints and the challenge of geographic origin determination, emphasizing the need for a more powerful discriminatory tool than can be formulated using current technology.

**Supplementary Materials:** The following are available online at <http://www.mdpi.com/2075-163X/10/5/447/s1>, Table S1: Elemental concentrations (ppm) of spot analyses of rubies and blue sapphires analyzed by LA-ICP-MS; Table S2: Trace element concentrations (ppm) in NIST SRM 614, NIST SRM 616, and corundum standard 02-1032-B analyzed by LA-ICP-MS; Table S3: Trace element abundances (ppm) and Sr and Pb isotopic ratios determined using offline LA followed by solution ICP-MS and TIMS for amphibolite- and marble-type ruby and metamorphic blue sapphires analyzed in this study. Quantification is achieved via normalization to the weight loss of the corundum crystals during ablation; Supplementary Material S4: LDA and PCA methodology and R runstreams, Supplementary Material S5: Summary of LDA results on LA-ICP-MS data, including error calculations, Supplementary Material S6: Sample classification codes.

**Author Contributions:** M.Y.K. performed the analyses, interpreted the results of the analyses, and wrote the manuscript. D.G.P. and M.Y.K. were responsible for the conception of this project. M.F.H. performed the statistical analyses and assisted with writing parts of the manuscript. Y.L. and C.S. provided technical input and assisted with the analyses. A.J.F. provided geology background and additional samples. All authors have read and agreed to the published version of the manuscript.

**Funding:** This research was primarily funded by a CERC award to Graham Pearson. The work was supported in part by the GIA R.T. Liddicoat Postdoctoral Fellowship.

**Acknowledgments:** The authors would like to thank Aaron Palke, of the Gemological Institute of America, for providing insight on sample gemology and fruitful discussions, and Sarah Woodland for assisting with measurements. In addition, the authors thank George Harlow, of the American Museum of Natural History, for providing samples from Myanmar, Vietnam, and Madagascar. Thank you to the three anonymous reviewers and the editors, Lin Sutherland and Khin Zaw, for providing constructive comments that improved this paper.

**Conflicts of Interest:** The authors declare no conflict of interest.

Appendix A

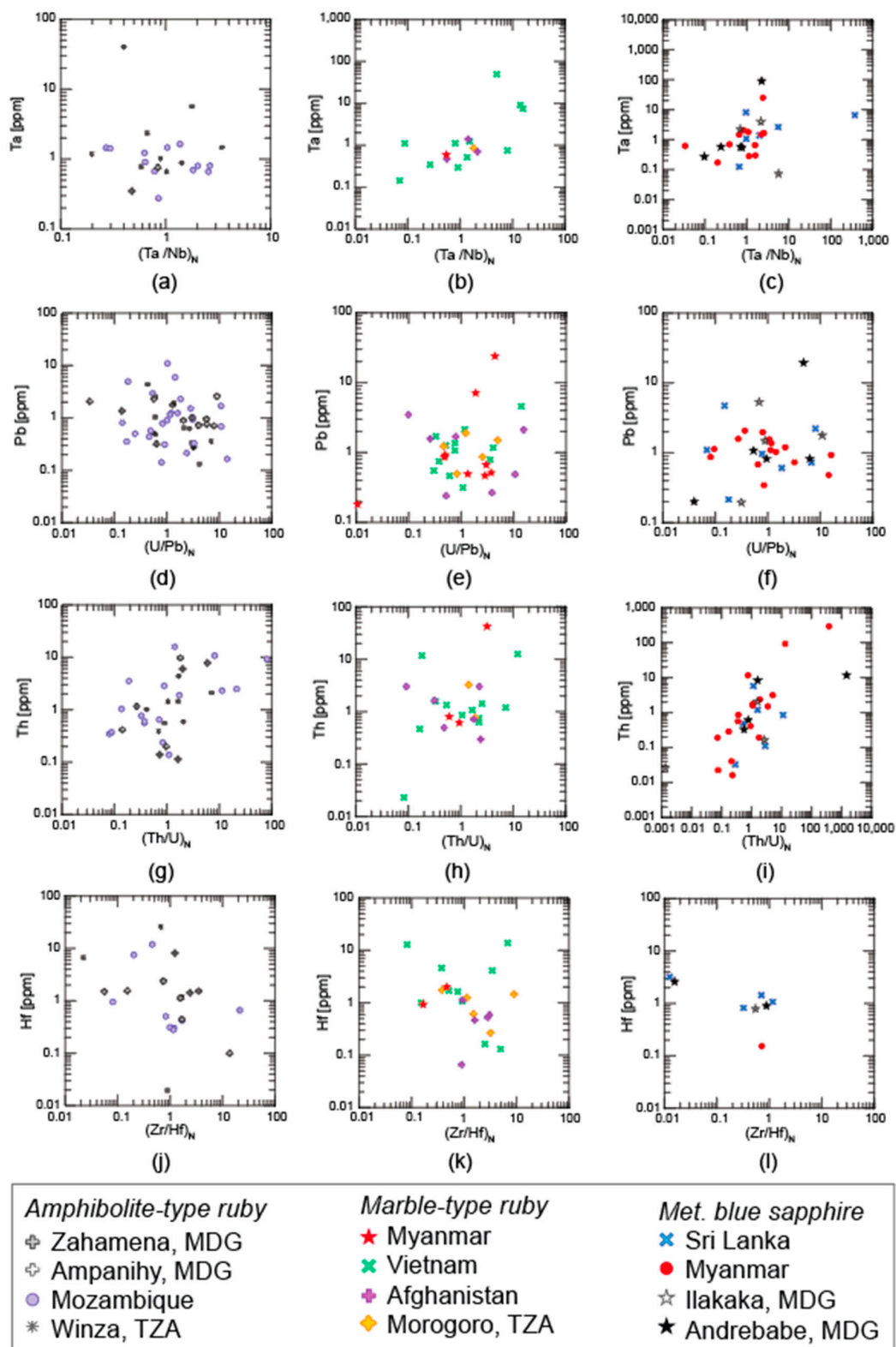


**Figure A1.** Primitive mantle-normalized [58] LA-ICP-MS data of gem corundum analyzed in this study. Points represent individual analyses. (a–c) Ta versus  $(Ta/Nb)_N$ ; (d–f) Pb versus  $(U/Pb)_N$ ; (g–i) Th versus  $(Th/U)_N$ , and (j–l) Hf versus  $(Zr/Hf)_N$  for amphibole-type ruby, marble-type ruby, and met. blue sapphire, respectively.

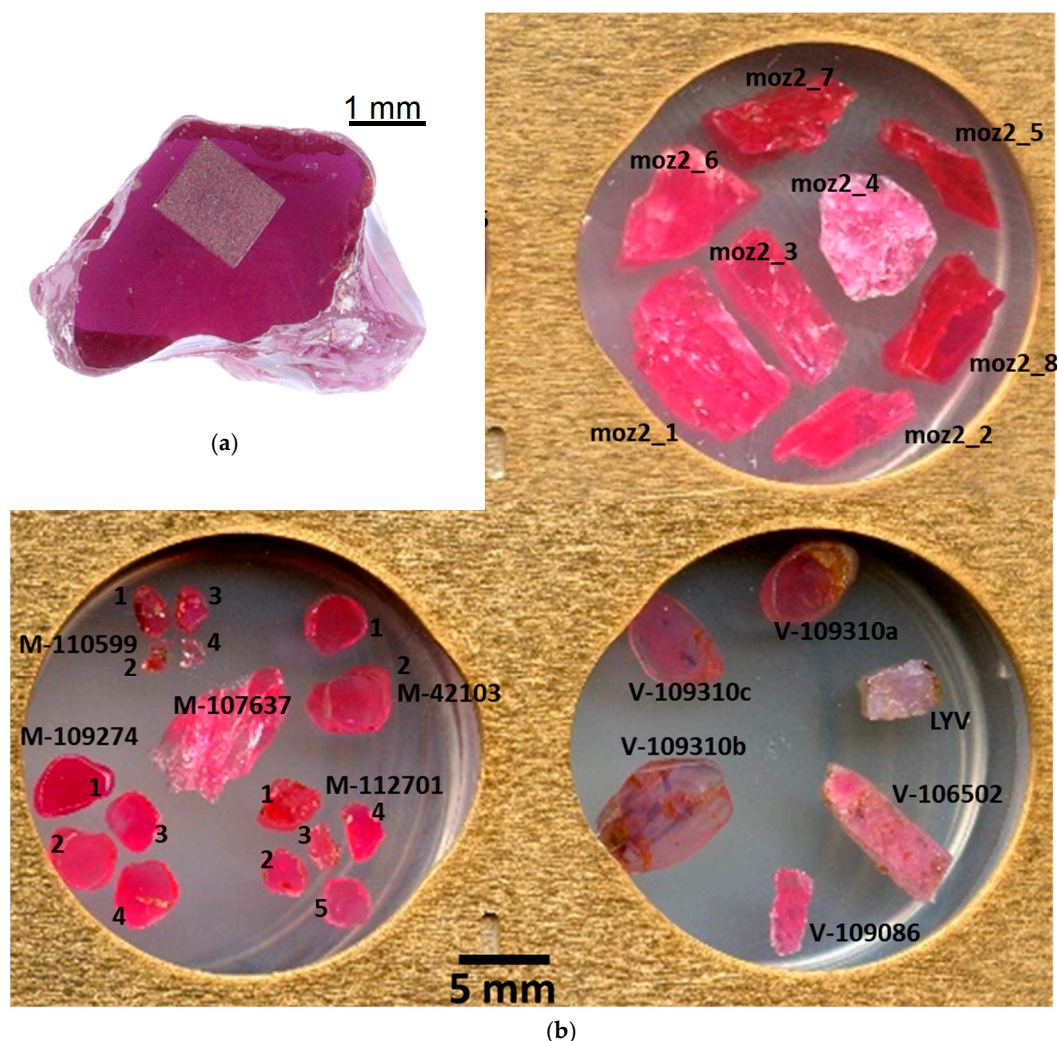


**Figure A2.** (a) Ruby from Zahamena, MDG after ablation clearly demonstrating the size of the offline ablation pit. (b) One inch resin sample mounts for LA-ICP-MS analysis showing rubies from Mozambique (moz), Myanmar (M-xxx), and Vietnam (V-xxx). A range of color and clarity is shown by these rubies.

## References

1. McClure, S.F.; Moses, T.M.; Shigley, J.E. The geographic origin dilemma. *Gems Gemol.* **2019**, *55*, 457–462.
2. Bui, H.A.N.; Fritsch, E.; Rondeau, B. Geographical origin: Branding or science. *InColor Mag.* **2012**, *19*, 30–39.
3. Cartier, L. Environmental stewardship in gemstone mining: Quo vadis? *InColor Mag.* **2010**, *15*, 9.
4. Palke, A.C.; Saeseaw, S.; Renfro, N.D.; Sun, Z.; McClure, S.F. Geographic origin determination of blue sapphire. *Gems Gemol.* **2019**, *55*, 536–579. [[CrossRef](#)]
5. Palke, A.C.; Saeseaw, S.; Renfro, N.D.; Sun, Z.; McClure, S.F. Geographic origin determination of ruby. *Gems Gemol.* **2019**, *55*, 580–613. [[CrossRef](#)]
6. The Gübelin Gemological Laboratory. A Holistic Method to Determining Gem Origin. 2006. Available online: [https://www.gubelingemlab.com/tl\\_files/content/03%20Gemmology/Gem%20Lab/Documents/Origin\\_Article\\_Sep2006.pdf](https://www.gubelingemlab.com/tl_files/content/03%20Gemmology/Gem%20Lab/Documents/Origin_Article_Sep2006.pdf) (accessed on 15 May 2020).
7. Giuliani, G.; Fallick, A.E.; Garnier, V.; France-Lanord, C.; Ohnenstetter, D.; Schwarz, D. Oxygen isotope composition as a tracer for the origins of rubies and sapphires. *Geology* **2005**, *33*, 249–252. [[CrossRef](#)]
8. Saminpaya, S.; Manning, D.A.C.; Droop, G.T.R.; Henderson, C.N.B. Trace elements in Thai gem corundums. *J. Gemmol.* **2003**, *28*, 399–416. [[CrossRef](#)]

9. Abduriyim, A.; Kitawaki, H. Applications of Laser Ablation—Inductively Coupled Plasma—Mass Spectrometry (LA-ICP-MS) to gemology. *Gems Gemol.* **2006**, *42*, 98–118. [[CrossRef](#)]
10. Peucat, J.J.; Ruffault, P.; Fritsch, E.; Bouhnik-Le Coz, M.; Simonet, C.; Lasnier, B. Ga/Mg ratio as a new geochemical tool to differentiate magmatic from metamorphic blue sapphires. *Lithos* **2007**, *98*, 261–274. [[CrossRef](#)]
11. Graham, I.T.; Sutherland, L.; Zaw, K.; Nechaev, V.; Khanchuk, A. Advances in our understanding of the gem corundum deposits of the West Pacific continental margins intraplate basaltic fields. *Ore Geol. Rev.* **2008**, *34*, 200–215. [[CrossRef](#)]
12. Krebs, M.Y.; Pearson, D.G.; Fagan, A.J.; Bussweiler, Y.; Sarkar, C. The application of trace elements and Sr–Pb isotopes to dating and tracing ruby formation: The Aappaluttoq deposit, SW Greenland. *Chem. Geol.* **2019**, *523*, 42–58. [[CrossRef](#)]
13. Dickin, A.P. *Radiogenic Isotope Geology*, 2nd ed.; Cambridge University Press: New York, NY, USA, 2005; ISBN 9780521823166.
14. Garnier, V.; Giuliani, G.; Ohnenstetter, D.; Schwarz, D. Saphirs et rubis. Classification des gisements de corindon. *Règne Minér.* **2004**, *55*, 4–47.
15. Muhlmeister, S.; Fritsch, E.; Shigley, J.E.; Devouard, B.; Laurs, B.M. Separating natural and synthetic rubies on the basis of trace-element chemistry. *Gems Gemol.* **1998**, *34*, 80–101. [[CrossRef](#)]
16. Kievenko, E.Y. *Geology of Gems*; Ocean Pictures Ltd.: Littleton, CO, USA, 2003.
17. Simonet, C.; Fritsch, E.; Lasnier, B. A classification of gem corundum deposits aimed towards gem exploration. *Ore Geol. Rev.* **2008**, *34*, 127–133. [[CrossRef](#)]
18. Giuliani, G.; Fallick, A.E.; Rakotondrazafy, M.; Ohnenstetter, D.; Andriamamonjy, A.; Ralantoarison, T.; Rakotosamizanany, S.; Razanatsheho, M.; Offant, Y.; Garnier, V.; et al. Oxygen isotope systematics of gem corundum deposits in Madagascar: Relevance for their geological origin. *Miner. Depos.* **2007**, *42*, 251–270. [[CrossRef](#)]
19. Stern, R.J.; Tsujimori, T.; Harlow, G.; Groat, L. Plate tectonic gemstones. *Geology* **2013**, *41*, 723–726. [[CrossRef](#)]
20. Giuliani, G.; Ohnenstetter, D.; Fallick, A.E.; Groat, L.A.; Fagan, A.J. The geology and genesis of gem corundum deposits. In *Mineralogical Association of Canada Short Course*; Mineralogical Association of Canada: Québec, QC, Canada, 2014; Volume 44, pp. 29–112.
21. Harlan, S.S. Timing of emplacement of the sapphire-bearing Yogo Dike, Little Belt Mountains, Montana. *Econ. Geol.* **1996**, *91*, 1159–1162. [[CrossRef](#)]
22. Verriest, W.; Palke, A.C.; Renfro, N.D. Field gemology: Building a research collection and understanding the development of gem deposits. *Gems Gemol.* **2019**, *55*, 490–511. [[CrossRef](#)]
23. Pardieu, V.; Sangsawong, S.; Muyl, J.; Chauviré, B.; Massi, L.; Sturman, N. Rubies from the Montepuez area (Mozambique). *GIA News*; Bangkok, Thailand, 2013. Available online: [https://www.gia.edu/doc/GIA\\_Ruby\\_Montepuez\\_Mozambique.pdf](https://www.gia.edu/doc/GIA_Ruby_Montepuez_Mozambique.pdf) (accessed on 10 May 2020).
24. Peretti, A.; Peretti, F.; Kanpraphai, A.; Bieri, W.P.; Mametner, K.; Guenther, D. *Winza Rubies Identified*, 2nd ed.; Peretti, A., Ed.; GRS Gem Research Swisslab: Lucerne, Switzerland, 2008; ISBN 9783952335970.
25. Schwarz, D.; Pardieu, V.; Saul, J.M.; Schmetzer, K.; Laurs, B.M.; Giuliani, G.; Klemm, L.; Malsy, A.; Erel, E.; Hauzenberger, C.; et al. Rubies and sapphires from Winza, Central Tanzania. *Gems Gemol.* **2008**, *44*, 322–347. [[CrossRef](#)]
26. Pardieu, V.; Sangsawong, S.; Detroyat, S. Rubies from a new deposit in Zahamena National Park, Madagascar. *Gems Gemol.* **2015**, *51*, 454–456.
27. Rakotondrazafy, A.F.M.; Giuliani, G.; Ohnenstetter, D.; Fallick, A.E.; Rakotosamizanany, S.; Andriamamonjy, A.; Ralantoarison, T.; Razanatsheho, M.; Offant, Y.; Garnier, V.; et al. Gem corundum deposits of Madagascar: A review. *Ore Geol. Rev.* **2008**, *34*, 134–154. [[CrossRef](#)]
28. Smith, C.P. Ruby and pink sapphire from Aappaluttoq, Greenland. *J. Gemmol.* **2016**, *35*, 294–306. [[CrossRef](#)]
29. Keulen, N.; Kalvig, P. Fingerprinting of corundum (ruby) from Fiskenaesset, West Greenland. *Geol. Surv. Den. Greenl. Bull.* **2013**, *28*, 53–56. [[CrossRef](#)]
30. Fagan, A.J. The Ruby and Pink Sapphire Deposits of SW Greenland: Geological Setting, Genesis, and Exploration Techniques. Ph.D. Thesis, The University of British Columbia, Vancouver, BC, Canada, 2018.
31. Fanka, A.; Sutthirat, C. Petrochemistry, mineral chemistry, and pressure—Temperature model of corundum-bearing amphibolite from Montepuez, Mozambique. *Arab. J. Sci. Eng.* **2018**, *43*, 3751–3767. [[CrossRef](#)]

32. Bowersox, G.W.; Foord, E.E.; Laurs, B.M.; Shigley, J.E.; Smith, C.P. Ruby and sapphire from Jegdalek, Afghanistan. *Gems Gemol.* **2000**, *36*, 110–126. [[CrossRef](#)]
33. Harlow, G.E.; Bender, W. A study of ruby (corundum) compositions from the Mogok Belt, Myanmar: Searching for chemical fingerprints. *Am. Miner.* **2013**, *98*, 1120–1132. [[CrossRef](#)]
34. Van Long, P.; Giuliani, G.; Fallick, A.E.; Boyce, A.J.; Pardieu, V. Trace elements and oxygen isotopes of gem spinels in marble from the Luc Yen—An Phu areas, Yen Bai province, North Vietnam. *Vietnam J. Earth Sci.* **2018**, *40*, 166–179.
35. Van Long, P.; Vinh, H.Q.; Garnier, V.; Giuliani, G.; Ohnenstetter, D.; Lhomme, T.; Schwarz, D.; Fallick, A.E.; Dubessy, J.; Trinh, P.T.; et al. Gem corundum deposits in Vietnam. *J. Gemmol.* **2004**, *29*, 129–147. [[CrossRef](#)]
36. Garnier, V.; Giuliani, G.; Ohnenstetter, D.; Fallick, A.E.; Dubessy, J.; Banks, D.; Vinh, H.Q.; Lhomme, T.; Maluski, H.; Pêcher, A.; et al. Marble-hosted ruby deposits from Central and Southeast Asia: Towards a new genetic model. *Ore Geol. Rev.* **2008**, *34*, 169–191. [[CrossRef](#)]
37. Haenni, H.A.; Schmetzer, K. New rubies from the Morogoro area, Tanzania. *Gems Gemol.* **1991**, *27*, 156–167. [[CrossRef](#)]
38. Balmer, W.A.; Hauzenberger, C.A.; Fritz, H.; Sutthirat, C. Marble-hosted ruby deposits of the Morogoro Region, Tanzania. *J. Afr. Earth Sci.* **2017**, *134*, 626–643. [[CrossRef](#)]
39. Kan-Nyunt, H.P.; Karampelas, S.; Link, K.; Thu, K.; Kiefert, L.; Hardy, P. Blue sapphires from the Baw Mar mine in Mogok. *Gems Gemol.* **2013**, *49*, 223–232. [[CrossRef](#)]
40. Hughes, E.B.; Perkins, R. Madagascar sapphire: Low-temperature heat treatment experiments. *Gems Gemol.* **2019**, *55*, 184–196. [[CrossRef](#)]
41. Guznawardene, M.; Rupasinghe, M.S. The elahera gem field in Central Sri Lanka. *Gems Gemol.* **1986**, *22*, 80–95. [[CrossRef](#)]
42. Atikarnsakul, U.; Vertriest, W.; Soonthorntantikul, W. Characterization of Blue Sapphires from the Mogok Stone Tract, Mandalay Region, Burma (Myanmar). *GIA News*. 19 June 2018, pp. 1–56. Available online: <https://www.gia.edu/doc/Characterization-of-blue-sapphires-from-the-Mogok-Stone-Tract-Mandalay-region-Burma-Myanmar.pdf> (accessed on 10 May 2020).
43. Soonthorntantikul, W.; Vertriest, W.; Raynaud-flattot, V.L.; Sangsawong, S. *An in-Depth Gemological Study of Blue Sapphires From the Baw Mar Mine (Mogok, Myanmar)*; GIA: Bangkok, Thailand, 2017.
44. Milisenda, C.C.; Henn, U.; Henn, J. New gemstone occurrences in the south-west of Madagascar. *J. Gemmol.* **2001**, *27*, 385–394. [[CrossRef](#)]
45. Pardieu, V.; Rakotosaona, N. *Ruby and Sapphire Rush Near Didy, Madagascar (April–June 2012)*; GIA: Bangkok, Thailand, 2012.
46. Dissanayake, C.B.; Chandrajith, R.; Tobschall, H.J. The geology, mineralogy and rare element geochemistry of the gem deposits of Sri Lanka. *Bull. Geol. Soc. Finl.* **2000**, *72*, 5–20. [[CrossRef](#)]
47. Pardieu, V.; Sangsawong, S.; Vertriest, W.; Detroyat, S.; Raynaud, V.; Engniwat, S. Blue sapphires from a new deposit near Andranondambo, Madagascar. *Gems Gemol.* **2016**, *52*, 96–97.
48. Schwarz, D.; Petsch, E.J.; Kanis, J. Sapphires from the Andranondambo Region, Madagascar. *Gems Gemol.* **1996**, *32*, 80–99. [[CrossRef](#)]
49. Stone-Sundberg, J.; Thomas, T.; Sun, Z.; Guan, Y.; Cole, Z.; Equall, R.; Emmett, J.L. Accurate reporting of key trace elements in ruby and sapphire using matrix-matched standards. *Gems Gemol.* **2017**, *53*, 438–451. [[CrossRef](#)]
50. Paton, C.; Hellstrom, J.; Paul, B.; Woodhead, J.; Hergt, J. Iolite: Freeware for the visualisation and processing of mass spectrometric data. *J. Anal. At. Spectrom.* **2011**, *26*, 2508. [[CrossRef](#)]
51. McNeill, J.; Pearson, D.G.; Klein-Bendavid, O.; Nowell, G.M.; Ottley, C.J.; Chinn, I. Quantitative analysis of trace element concentrations in some gem-quality diamonds. *J. Phys. Condens. Matter* **2009**, *21*, 364207. [[CrossRef](#)]
52. Klein-BenDavid, O.; Pearson, D.G.; Nowell, G.M.; Ottley, C.; McNeill, J.C.R.; Cartigny, P. Mixed fluid sources involved in diamond growth constrained by Sr-Nd-Pb-C-N isotopes and trace elements. *Earth Planet. Sci. Lett.* **2010**, *289*, 123–133. [[CrossRef](#)]
53. Krebs, M.Y.; Pearson, D.G.; Stachel, T.; Laiginhas, F.; Woodland, S.; Chinn, I.; Kong, J. A common parentage-low abundance trace element data of gem diamonds reveals similar fluids to fibrous diamonds. *Lithos* **2019**, 324–325. [[CrossRef](#)]

54. Charlier, B.L.A.; Ginibre, C.; Morgan, D.; Nowell, G.M.; Pearson, D.G.; Davidson, J.P.; Ottley, C.J. Methods for the microsampling and high-precision analysis of strontium and rubidium isotopes at single crystal scale for petrological and geochronological applications. *Chem. Geol.* **2006**, *232*, 114–133. [[CrossRef](#)]
55. Harlou, R.; Pearson, D.G.; Nowell, G.M.; Ottley, C.J.; Davidson, J.P. Combined Sr isotope and trace element analysis of melt inclusions at sub-ng levels using micro-milling, TIMS and ICPMS. *Chem. Geol.* **2009**, *260*, 254–268. [[CrossRef](#)]
56. Sarkar, C.; Pearson, D.G.; Heaman, L.M.; Woodland, S.J. Precise Pb isotope ratio determination of picogram-size samples: A comparison between multiple Faraday collectors equipped with  $10^{12}\Omega$  amplifiers and multiple ion counters. *Chem. Geol.* **2015**, *395*, 27–40. [[CrossRef](#)]
57. Todt, W.; Cliff, R.A.; Hanser, A.; Hofmann, A.W. Evaluation of a  $^{202}\text{Pb}$ – $^{205}\text{Pb}$  double spike for high-precision lead isotope analysis. In *Earth Processes: Reading the Isotopic Code*; Basu, A., Hart, S.R., Eds.; American Geophysical Union Geophysical Monograph: Washington, DC, USA, 1996; pp. 429–437.
58. McDonough, W.F.; Sun, S.-S. The composition of the earth. *Chem. Geol.* **1995**, *120*, 223–253. [[CrossRef](#)]
59. Pornwilard, M.M.; Hansawek, R.; Shiowatana, J.; Siripinyanond, A. Geographical origin classification of gem corundum using elemental fingerprint analysis by laser ablation inductively coupled plasma mass spectrometry. *Int. J. Mass Spectrom.* **2011**, *306*, 57–62.
60. Sutherland, F.; Zaw, K.; Meffre, S.; Yui, T.-F.; Thu, K. Advances in trace element “Fingerprinting” of gem corundum, ruby and sapphire, Mogok Area, Myanmar. *Minerals* **2014**, *5*, 61–79. [[CrossRef](#)]
61. Sutherland, F.L.; Abduriyim, A. Geographic typing of gem corundum: A test case from Australia. *J. Gemmol.* **2009**, *31*, 203–210. [[CrossRef](#)]
62. Sutherland, F.; Zaw, K.; Meffre, S.; Thompson, J.; Goemann, K.; Thu, K.; Nu, T.; Zin, M.; Harris, S. Diversity in ruby geochemistry and its inclusions: Intra- and inter-continental comparisons from Myanmar and Eastern Australia. *Minerals* **2019**, *9*, 28. [[CrossRef](#)]
63. Sutherland, F.L.; Zaw, K.; Meffre, S.; Giuliani, G.; Fallick, A.E.; Graham, I.T.; Webb, G.B. Gem-corundum megacrysts from east Australian basalt fields: Trace elements, oxygen isotopes and origins. *Aust. J. Earth Sci.* **2009**, *56*, 1003–1022. [[CrossRef](#)]
64. Zaw, K.; Sutherland, L.; Yui, T.F.; Meffre, S.; Thu, K. Vanadium-rich ruby and sapphire within Mogok Gemfield, Myanmar: Implications for gem color and genesis. *Miner. Depos.* **2014**, *50*, 25–39. [[CrossRef](#)]
65. Sutherland, F.L.; Piilonen, P.C.; Zaw, K.; Meffre, S.; Thompson, J. Sapphire within zircon-rich gem deposits, Bo Loei, Ratanakiri Province, Cambodia: Trace elements, inclusions, U–Pb dating and genesis. *Aust. J. Earth Sci.* **2015**, *62*, 761–773.
66. Sutherland, F.L.; Graham, I.T.; Harris, S.J.; Coldham, T.; Powell, W.; Belousova, E.A.; Martin, L. Unusual ruby–sapphire transition in alluvial megacrysts, Cenozoic basaltic gem field, New England, New South Wales, Australia. *Lithos* **2017**, *278–281*, 347–360. [[CrossRef](#)]
67. Sorokina, E.S.; Rassomakhin, M.A.; Nikandrov, S.N.; Karampelas, S.; Kononkova, N.N.; Nikolaev, A.G.; Anosova, M.O.; Somsikova, A.V.; Kostitsyn, Y.A.; Kotlyarov, V.A.; et al. Origin of blue sapphire in newly discovered spinel–chlorite–muscovite rocks within meta-ultramafites of ilmen mountains, South Urals of Russia: Evidence from mineralogy, geochemistry, RB–SR and Sm–Nd isotopic data. *Minerals* **2019**, *9*, 36. [[CrossRef](#)]
68. Graham, I.T.; Harris, S.J.; Martin, L.; Lay, A.; Zappettini, E. Enigmatic alluvial sapphires from the Orosmayo Region, Jujuy Province, Northwest Argentina: Insights into their origin from in situ oxygen isotopes. *Minerals* **2019**, *9*, 390. [[CrossRef](#)]
69. Cartier, L.E. Ruby and sapphire from Marosely, Madagascar. *J. Gemmol.* **2009**, *31*, 171–180. [[CrossRef](#)]
70. Baldwin, L.C.; Ballhaus, F.T.C.; Fonseca, A.G.R.O.C. Petrogenesis of alkaline basalt-hosted sapphire megacrysts. Petrological and geochemical investigations of in situ sapphire occurrences from the Siebengebirge Volcanic Field, Germany. *Contrib. Miner. Pet.* **2017**, *172*, 1–27. [[CrossRef](#)]
71. Guillong, M.; Günther, D. Quasi “non-destructive” laser ablation-inductively coupled plasma-mass spectrometry fingerprinting of sapphires. *Spectrochim. Acta-Part B At. Spectrosc.* **2001**, *56*, 1219–1231. [[CrossRef](#)]
72. Boyd, R.; Nordgulen, O.; Thomas, R.J.; Bingen, B.; Bjerkgård, T.; Grenne, T.; Henderson, I.; Melezhik, V.A.; Often, M.; Sandstad, J.S.; et al. The geology and geochemistry of the East African orogen in northeastern Mozambique. *S. Afr. J. Geol.* **2010**, *113*, 87–129. [[CrossRef](#)]

73. Barley, M.E.; Pickard, A.L.; Zaw, K.; Rak, P.; Doyle, M.G. Jurassic to Miocene magmatism and metamorphism in the Mogok metamorphic belt and the India-Eurasia collision in Myanmar. *Tectonics* **2003**, *22*, 22. [[CrossRef](#)]
74. Searle, M.P.; Noble, S.R.; Cottle, J.M.; Waters, D.J.; Mitchell, A.H.G.; Hlaing, T.; Horstwood, M.S.A. Tectonic evolution of the Mogok metamorphic belt, Burma (Myanmar) constrained by U-Th-Pb dating of metamorphic and magmatic rocks. *Tectonics* **2007**, *26*, 26. [[CrossRef](#)]
75. Silva, K.K.M.W.; Siriwardena, C.H.E.R. Geology and the origin of the corundum-bearing skarn at Bakamuna, Sri Lanka. *Miner. Depos.* **1988**, *23*, 186–190. [[CrossRef](#)]
76. Thu, K. The Igneous Rocks of the Mogok Stone Tract. Ph.D. Thesis, University of Yangon, Yangon, Myanmar, 2007.



© 2020 by the authors. Licensee MDPI, Basel, Switzerland. This article is an open access article distributed under the terms and conditions of the Creative Commons Attribution (CC BY) license (<http://creativecommons.org/licenses/by/4.0/>).